

RADIO SOURCES IN THE NEARBY UNIVERSE

J. J. CONDON¹

National Radio Astronomy Observatory, 520 Edgemont Road, Charlottesville, VA 22903, USA

A. M. MATTHEWS

Department of Astronomy, University of Virginia, Charlottesville, VA 22904, USA

AND

J. J. BRODERICK

Department of Physics, Virginia Polytechnic Institute and State University, Blacksburg, VA 24061, USA

Draft version January 30, 2019

ABSTRACT

We identified 15,658 NVSS radio sources among the 55,288 2MASX galaxies brighter than $k_{20fe} = 12.25$ at $\lambda = 2.16 \mu\text{m}$ and covering the $\Omega = 7.016$ sr of sky defined by J2000 $\delta > -40^\circ$ and $|b| > 20^\circ$. The complete sample of 15,043 galaxies with 1.4 GHz flux densities $S \geq 2.45$ mJy contains a 99.9% spectroscopically complete subsample of 9,517 galaxies with $k_{20fe} \leq 11.75$. We used only radio and infrared data to quantitatively distinguish radio sources powered primarily by recent star formation from those powered by active galactic nuclei. The radio sources with $\log[L(\text{W Hz}^{-1})] > 19.3$ that we used to derive the local spectral luminosity and power-density functions account for $> 99\%$ of the total 1.4 GHz spectral power densities $U_{\text{SF}} = (1.54 \pm 0.20) \times 10^{19} \text{ W Hz}^{-1} \text{ Mpc}^{-3}$ and $U_{\text{AGN}} = (4.23 \pm 0.78) \times 10^{19} \text{ W Hz}^{-1} \text{ Mpc}^{-3}$ in the universe today, and the spectroscopic subsample is large enough that the quoted errors are dominated cosmic variance. The recent comoving star-formation rate density indicated by U_{SF} is $\psi \approx 0.015 M_\odot \text{ yr}^{-1} \text{ Mpc}^{-3}$.

Keywords: catalogs — galaxies: active — galaxies: luminosity function, mass function — galaxies: star formation — infrared: galaxies — radio continuum: galaxies

1. INTRODUCTION

The 1.4 GHz continuum emission from galaxies is powered by a combination of recent star formation in star-forming galaxies (SFGs) and supermassive black holes (SMBHs) in active galactic nuclei (AGNs). The tight and nearly linear far-infrared (FIR)/radio correlation observed among low-redshift galaxies makes 1.4 GHz spectral luminosity a good dust-unbiased tracer proportional to the recent star-formation rate (SFR) (Condon 1992), while sources that are radio-loud relative to the FIR/radio correlation reveal the presence of radio-dominant AGNs, even those deeply embedded in dust.

This paper presents separate local radio luminosity functions for both source types. When used in conjunction with sensitive radio surveys made by the JVLA, MeerKAT, the SKA, or the ngVLA, local luminosity functions anchor models for the cosmological co-evolution of star formation and SMBH growth. Our large ($N = 9,517$) spectroscopically complete sample of the brightest ($k_{20fe} \leq 11.75$ and $S_{1.4 \text{ GHz}} \geq 2.45$ mJy) galaxies covers most of the extragalactic sky ($\Omega = 7.016$ sr) in order to (1) reach the low radio spectral luminosities $\log[L_{1.4 \text{ GHz}}(\text{W Hz}^{-1})] \geq 19.3$ needed to constrain the full range of sources accounting for nearly all ($> 99\%$) recent star formation and SMBH growth and (2) minimize cosmic variance.

Bright galaxies are also more likely to have the multiwavelength data needed to distinguish between radio sources powered by star formation and by AGNs. The total radio emission from any galaxy is actually the sum of both types, so quantitatively accurate criteria are needed to determine which is dominant. We used only quantitative FIR, MIR (mid-infrared), and radio data to determine which type is energetically dominant. We did not use BPT diagrams (Baldwin et al. 1981) or other optical emission-line diagnostics because they are not good *quantitative* measures of AGN-powered radio emission. It turns out, however, that the Mauch & Sadler (2007) AGN/SFG classifications based on optical spectra agree surprisingly well with ours.

The cosmological evolution of radio sources is so strong that nearby sources comprise only a small fraction of all sources in flux-limited samples. Radio continuum emission alone cannot separate the nearby needles from the haystack of distant sources, so statistically complete and reliable samples of nearby radio sources are usually selected by position-coincidence cross-identifications with optical or infrared samples of bright galaxies. For example, of all NRAO VLA Sky Survey (NVSS) (Condon et al. 1998) sources stronger than $S \approx 2.5$ mJy at $\nu = 1.4$ GHz, $< 1\%$ can be identified with galaxies brighter than $m_p = 14.5$ (Condon et al. 2002). About 85% of those sources are in relatively low-luminosity star-forming galaxies (SFGs) whose median face-on surface brightness is just $\langle T_b \rangle \sim 1$ K at $\nu = 1.4$ GHz (Hummel 1981), so reasonably complete samples of nearby radio sources can be constructed only from radio surveys hav-

jcondon@nrao.edu
amm4ws@virginia.edu

¹The National Radio Astronomy Observatory is a facility of the National Science Foundation operated under cooperative agreement by Associated Universities, Inc.

ing lower surface-brightness detection limits. The NVSS is suitable because its sensitivity limit is $T_b = 5\sigma_T \approx 0.7$ K.

This paper presents and analyzes a large catalog of NVSS sources identified with 2 Micron All-Sky Survey eXtended (2MASX) galaxies (Jarrett et al. 2000) brighter than $k_{20fe} = 12.25$ at $\lambda = 2.16 \mu\text{m}$, where k_{20fe} is the magnitude measured inside the 20 mag arcsec⁻² isophote. The 2MASX galaxy sample is described in Section 2, and the NVSS radio identification procedure is explained in Section 3. The resulting 2MASX/NVSS catalog (Section 4) contains a statistically complete sample of 15,043 galaxies brighter than $k_{20fe} = 12.25$ and 1.4 GHz flux densities $S \geq 2.45$ mJy. Most of the analysis in this paper is based on the spectroscopically complete subsample of 9,517 galaxies with $k_{20fe} \leq 11.75$ and $S \geq 2.45$ mJy. All but 19 had published spectroscopic redshifts, and we measured new spectroscopic redshifts for 12 of the 19 (Appendix B). Only FIR, MIR (mid-infrared), and radio data were used to distinguish 2MASX/NVSS radio sources primarily powered by recent star formation from those dominated by AGNs (Section 4.1). The counts of 2MASX/NVSS sources powered by star formation and AGNs as functions of 1.4 GHz flux density are plotted and discussed in Section 4.2. Separate 1.4 GHz local luminosity functions for SFGs and AGNs are reported in Section 6, and Section 7 presents the corresponding spectral power density functions. Cosmic variance exceeds the Poisson variance for the large 2MASX/NVSS spectroscopic sample (Section 8). The total 1.4 GHz spectral energy density produced by SFGs today, $U_{\text{SF}} = (1.54 \pm 0.20) \times 10^{19}$ W Hz⁻¹ Mpc⁻³, indicates that the recent SFRD is $\psi \approx 0.015 M_{\odot} \text{ yr}^{-1} \text{ Mpc}^{-3}$.

All calculations of absolute quantities (comoving distance, spectral luminosity, ...) from the observables (redshift, flux density, ...) are based on the relativistically correct equations for a Λ CDM universe from Condon & Matthews (2018) with $\Omega_m = 0.3$, $\Omega_{\Lambda} = 0.7$, and $H_0 = 70 \text{ km s}^{-1} \text{ Mpc}^{-1}$ ($h = 0.70$).

2. THE 2MASX GALAXY SAMPLE

Large samples of bright galaxies necessarily cover a significant fraction of the sky. The Two Micron All Sky Survey (2MASS) (Skrutskie et al. 2006) Extended Source Catalog (2MASX) (Jarrett et al. 2000) is ideal because:

(1) It is complete and reliable over the whole extragalactic sky for galaxies brighter than $k_s \approx k_{20fe} + 0.2 \approx 13.5$ ($S_{2.16 \mu\text{m}} \approx 2.9$ mJy) at the longest infrared wavelength ($\lambda \approx 2.16 \mu\text{m}$) yielding good atmospheric transparency. Dust extinction in our Galaxy and dust absorption in nearby galaxies are both small at this wavelength, and confusion by stars is negligible at galactic latitudes $|b| \geq 20^\circ$.

(2) The $\lambda = 2.16 \mu\text{m}$ luminosity of a normal galaxy is nearly proportional to its total stellar mass (Bell et al. 2003) because dust absorption is low and late-type stars dominate the near-infrared (NIR) luminosity. Thus the 2MASX sample most directly samples the stellar masses in galaxies; it is less biased than optical or FIR samples by recently formed massive stars. The NVSS/2MASX flux-density ratio is a good measure of the recent star formation rate per unit stellar mass, or the specific star-

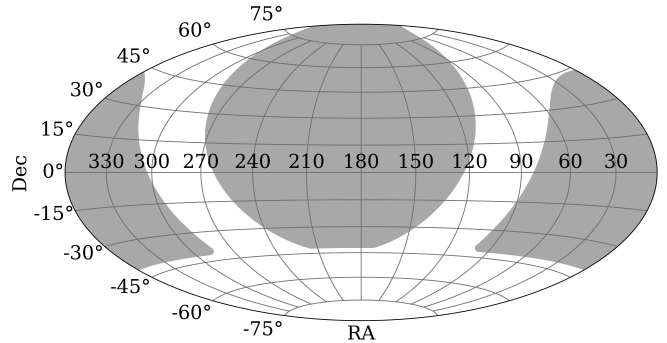


Figure 1. The shaded 2MASX/NVSS area in this equal-area Hammer projection covers the $\Omega \approx 7.016$ sr (56% of the sky) with J2000 $\delta > -40^\circ$ and absolute galactic latitude $|b| > 20^\circ$.

formation rate (SSFR), which is a constraint on the star-formation history of the universe.

(3) The 2MASX photometric errors for galaxies brighter than $k_s \sim 12.5$ are $\lesssim 4\%$.

(4) Nearly all 2MASX galaxies have such small absolute position errors ($< 1''$ rms) that complete and reliable radio identifications of 2MASX galaxies can be made by position coincidence alone.

(5) Spectroscopic redshifts are now available for nearly all galaxies brighter than $k_{20fe} = 11.75$ (Huchra et al. 2012).

Our 2MASX galaxy sample includes all galaxies with: (1) 2MASX catalog fiducial magnitudes $k_{20fe} \leq 12.25$ mag measured within the 20 mag arcsec⁻² ($\approx 3\sigma$) fiducial elliptical aperture. According to the 2MASS Explanatory Supplement (<https://www.ipac.caltech.edu/penalty/z@2mass/releases/allsky/penalty/z@doc/explsup.html>), the measured fiducial flux density typically contains about 85% of the extrapolated total flux density.

(2) 2MASX fiducial semi-major axes $r_{20fe} \geq 5''$, above which the 2MASX catalog is nominally complete, and (3) J2000 $\delta > -40^\circ$, the NVSS southern declination limit, and absolute galactic latitude $|b| > 20^\circ$, the limit of the *InfraRed Astronomical Satellite (IRAS)* Faint Source Catalog (FSC) (Moshir et al. 1992). This $\Omega \approx 7.016$ sr (Appendix A) sky area is shown in Figure 1.

The 2MASX all-sky data release catalog (<https://www.ipac.caltech.edu/2mass/releases/allsky/>) contains $N_{\text{IR}} = 55,288$ infrared galaxies satisfying all three requirements. Their mean sky density is $\rho_{\text{IR}} \approx 2.40 \text{ deg}^{-2}$.

3. NVSS IDENTIFICATIONS OF 2MASX GALAXIES

To find all plausible NVSS identification candidates for the 2MASX galaxies, we used the NVSS catalog browser (<http://www.cv.nrao.edu/nvss/NVSSlist.shtml>) to select the 18,360 2MASX sample galaxies having (1) at least one NVSS radio component within a search radius $r_s = 60''$ or (2) at least 2 NVSS components within $r_s = 120''$. These search radii are compromises large enough to ensure high completeness but small enough to avoid including too many unrelated background sources. Note that the NVSS catalog lists elliptical Gaussian radio *components* fitted to peaks on NVSS images, so the extended radio *source* produced by one galaxy may be represented by more than one radio component. If the

radio emission from a galaxy is confused, asymmetric, or significantly larger than the $\theta = 45''$ FWHM Gaussian NVSS beam, the radio positions may be significantly offset from the host galaxy position. This is the case for $\sim 5\%$ of 2MASX/NVSS galaxies, so initial search radii much larger than the combined 2MASX and NVSS position errors are needed to capture all radio identifications and include all of their radio emission.

Our large search areas contain an unacceptable number of unrelated background sources because the mean sky density of NVSS components is $\rho \approx 53 \text{ deg}^{-2}$. The rms statistical sampling error in a catalog of $N \sim 10^4$ identifications is $N^{1/2} \sim 10^2$, so exploiting the statistical power of such a large catalog requires identification reliability $\gtrsim 99\%$. Most background radio sources are so distant (mean $\langle z \rangle \sim 1$) that they are quite randomly distributed on the sky. Thus the Poisson probability P that one or more unrelated NVSS components will lie within $r_s = 60''$ of any 2MASX galaxy is

$$P(\geq 1) = 1 - P(0) = 1 - \exp(-\pi\rho r_s^2) \approx 0.045, \quad (1)$$

where the mean number of unrelated components in a search circle is $\mu = \pi\rho r_s^2$ and the probability of finding none is $P(0) = \exp(-\mu)$. In addition, some 2MASX galaxies are members of physical groups and clusters, so the radio emission from close companion galaxies must be excluded. Thus *at least* $N_{\text{IR}}P(\geq 1) = 55,288 \times 0.045 \gtrsim 2500$ of the 18360 candidate fields with $r_s = 60''$ are likely to contain unrelated NVSS components, leaving $\lesssim 16,000$ genuine 2MASX/NVSS identifications. The probability of finding two or more background sources within $r_s = 120''$ is

$$\begin{aligned} P(\geq 2) &= 1 - P(0) - P(1) \\ &= 1 - (1 - \pi\rho r_s^2) \exp(-\pi\rho r_s^2) \approx 0.015. \end{aligned} \quad (2)$$

Genuine 2MASX/NVSS identifications with neither a single component within $60''$ nor two or more components within $120''$ are rare but may have been missed.

Recognizing and weeding out the background sources required extensive and time-consuming human intervention, as described below.

Most of the radio sources produced by bright 2MASX galaxies are fairly compact or at least symmetric. Nearly all 2MASX galaxies have rms position errors $\sigma_\alpha \approx \sigma_\delta \ll 1''$, and NVSS position errors for unresolved components decline with catalog flux density from $\sigma_\alpha \approx \sigma_\delta \approx 5''$ at $S = 2.45 \text{ mJy}$ to $\lesssim 1''$ for $S > 15 \text{ mJy}$. Such candidates can be reliably accepted or rejected on the basis position coincidence alone. We define σ as the quadratic sum of the 2MASX and NVSS rms position errors in each coordinate,

$$m \equiv r_s / \sigma \quad (3)$$

as the identification search radius in units of σ , and

$$k \equiv 1 + 2\pi\rho\sigma^2. \quad (4)$$

For $\rho = 53 \text{ deg}^{-2} \approx 4.09 \times 10^{-6} \text{ arcsec}^{-2}$ and the worst case $\sigma \approx 5''$, $k \approx 1.000642$. In terms of m and k the completeness of the identifications is (Condon et al. 1975)

$$C = \frac{1 - \exp(-m^2k/2)}{k}. \quad (5)$$

Even when $\sigma = 5''$, $m = 3$ ($r_s = 15''$) ensures $C \approx 0.99$. The fraction of 2MASX galaxies actually having NVSS counterparts is $f \approx 15,658/55,288 \approx 0.3$. The identification reliability (Condon et al. 1975)

$$R = C \left[\frac{1}{f} + \left(1 - \frac{1}{f} \right) \exp[m^2(1-k)/2] - \exp\left(-\frac{m^2k}{2}\right) \right]^{-1} \quad (6)$$

is also $\gtrsim 99\%$ because the probability that an unrelated NVSS source lies within $3\sigma \approx 15''$ of any position is < 0.003 .

Figures 2 and 3 present examples illustrating both typical and difficult 2MASX/NVSS cross-identifications. The upper left panel of Figure 2 shows the Digitized Sky Survey (DSS) gray-scale optical image, the NVSS 1.4 GHz brightness contours, and the *IRAS* 2σ position error ellipse for the typical spiral galaxy IC 1526. Its 1.4 GHz flux density $S = 5.4 \pm 0.5 \text{ mJy}$ and its 2MASX/NVSS position offset $r = 3''.8$ ($m = 1.3$) are close to the sample medians. The radio sources in nearly all spiral galaxies are fairly symmetric and roughly coextensive with their optical host galaxies of stars.

Nonetheless, some radio sources in spiral galaxies could not be found by position coincidence alone. In the upper right panel of Figure 2, the confused 2MASX position of NGC 5668 is marked by the cross on a bright spot $\sim 22''$ north of the galaxy nucleus. A few large face-on and edge-on spiral galaxies have significantly offset or even multiple 2MASX positions that can be recognized most easily by visual inspection of finding charts like this one.

The NVSS contours and accurate 2MASX position for the very extended low-brightness galaxy M74 are shown in the middle row, left panel of Figure 2. The closest NVSS catalog component is $93''$ from the 2MASX position, so M74 is not in the list of candidates within the $r_s = 60''$ search radius. To find similar cases, we searched for identifications among all galaxies in the 1.49 GHz atlas of spiral galaxies with $B_T \leq 12$ (Condon 1987). M74 emphasizes the importance of high surface-brightness sensitivity for identifying reasonably complete radio samples of nearby galaxies. Its total 1.4 GHz flux density is $S \approx 180 \text{ mJy}$, but its surface brightness is barely above the NVSS $5\sigma \approx 5 \times 0.45 \text{ mJy beam}^{-1} \approx 2.3 \text{ mJy beam}^{-1}$ detection limit.

The price of high brightness sensitivity is low angular resolution. The $\theta = 45''$ NVSS beam only marginally resolves the pair of galaxies UGC 00644 and UGC 00644 NOTES01 (Figure 2 middle row, right panel), and the NVSS catalog lists only a single extended Gaussian component whose radio centroid position is midway between the galaxies. Finding charts make it easy for humans to recognize such blends and decompose the radio sources into unresolved components on the galaxy positions.

The majority of AGN-powered radio galaxies are also sufficiently compact and/or symmetric to permit simple position-coincidence identifications. The lower left panel of Figure 2 shows the radio emission from an anonymous $S = 15.0 \text{ mJy}$ (about the median flux density of AGNs in the sample) galaxy. However, a significant minority of low-luminosity radio galaxies are distinctly asymmetric. In the lower right panel in Figure 2 are the 2MASX position cross and NVSS contours of a head-tail radio galaxy whose centroid is significantly offset to the north.

The head-tail morphology of this source is confirmed by the high-resolution VLA image of Owen et al. (1993). Slightly bent radio jets are common, but truly one-sided radio jets are rare in low-luminosity radio sources. The radio galaxy IC 1695 in the cluster Abell 0193 appears in the upper left panel of Figure 3. About half of its flux density arises from a compact component in the galaxy, and half originates in a slightly curved one-sided jet extending $\sim 1'$ to the northeast (Owen & Ledlow 1997).

Radio galaxies powered by AGNs may emit most or even all of their power in jets and lobes lying well outside the host galaxies of stars. Thus it is necessary to search for radio components quite far from each 2MASX position, *whether or not* there is a radio component close to the 2MASX position. The right panel in the top row of Figure 3 is centered on an anonymous elliptical galaxy at redshift $z \approx 0.0885$, so this $6' \times 6'$ finding chart is ≈ 640 kpc on a side and the triple radio source is even larger. Mauch & Sadler (2007) identified only the $S = 17.5$ mJy central NVSS component with the 2MASX galaxy, even though other NVSS components lie within their $r_s = 3'$ candidate search radius and yield a total flux density $S \approx 680$ mJy. Sources like this are difficult to recognize from component lists alone; there is no substitute for visual inspection of finding charts that extend at least $\pm 3'$ in both directions. The much larger $\pm 8'$ finding chart in the left panel, middle row of Figure 3 is centered on the $S \approx 430$ mJy triple radio galaxy 2MASX J15280499+0544278. Only the $S = 45.1$ mJy central component was identified by Best & Heckman (2012), and the lobes are only partially visible and not easily recognized on our usual $6' \times 6'$ finding chart, so we might have missed other sources with even more widely separated lobes. Although large triple sources like these are rare among bright galaxies, they are usually so luminous that capturing their total flux densities is important for deriving accurate radio luminosity functions.

Some “empty double” radio sources have no NVSS components within $60''$ of their 2MASX host galaxies. To find them, we searched for pairs or multiple components offset by up to $120''$. The nearest NVSS components in the X-shaped radio source 4C +32.25 = B2 0828+32 (right panel, middle row of Figure 3) are the bright FR II lobes symmetrically offset from 2MASX J08312752+3219270 by $104''$ and $119''$. The larger but fainter north-south extension has a steep radio spectrum and may be the relic of an earlier outburst in a precessing system (Parmi et al. 1985). Most coreless double sources can be recognized because their lobes have roughly equal flux densities, are about equally distant from their host galaxies, and are at position angles differing by $\sim 180^\circ$. Somewhat more difficult to recognize are bent coreless doubles. The left panel, bottom row of Figure 3 shows the luminous ($S \approx 650$ mJy at $z \approx 0.0830$) bent double source having no NVSS components within $60''$ of the cross on 2MASX J08284360+2437220. Finally, the lower right panel of Figure 3 shows a large but faint double source that illustrates the limit of reliable identifications. Secondary evidence supporting this identification as a double source includes (1) the two components are roughly equidistant from the 2MASX galaxy, (2) the two components have comparable brightness, (3) the line between them passes close to the galaxy, and (4) the southwest component has a tail pointing back toward

the galaxy.

4. THE 2MASX/NVSS CATALOG AND SAMPLES

Following the procedures described in Section 3, we identified NVSS sources with 15,658 of the 55,288 2MASX galaxies having $k_{20\text{fe}} \leq 12.25$ and semi-major axes $r_{20\text{fe}} \geq 5''$ in the $\Omega \approx 7.016$ sr solid angle defined by J2000 declination $\delta > -40^\circ$ and absolute galactic latitude $|b| \geq 20^\circ$. The resulting 2MASX/NVSS galaxy catalog is displayed in part as Table 1, which lists for each galaxy its 2MASX J2000 coordinate name, 2MASX fiducial $\lambda = 2.16 \mu\text{m}$ magnitude $k_{20\text{fe}}$, 2MASX fiducial major-axis diameter $d_{20\text{fe}} = 2r_{20\text{fe}}$ in arcsec, 1.4 GHz NVSS total flux density S in mJy, dominant radio energy source type (either recent star formation S or active galactic nucleus A) derived from FIR data, from MIR data, and the final type derived from both as explained in Section 4.1, heliocentric radial velocity cz in km s^{-1} usually from the NASA/IPAC Extragalactic Database (NED), and the most common alternative galaxy name (e.g., UGC 12890) from NED.

All NVSS catalog flux densities are rounded to the nearest 0.1 mJy, so the 15,043 galaxies with 1.4 GHz catalog flux densities $S \geq 2.5$ mJy comprise a flux-limited sample complete to $\bar{S} = 2.45$ mJy. The spectroscopically complete subsample of the 9,517 galaxies with $k_{20\text{fe}} \leq 11.75$ and $S \geq 2.45$ mJy now has redshifts for all but 7 (99.9% redshift completeness).

4.1. Radio Energy Sources

The ultimate energy sources powering the radio continuum emission from galaxies are recently formed massive short-lived stars and SMBHs in AGNs. In order to use radio continuum luminosity as a quantitative tracer of the SFR, we classified the radio emission of each galaxy in Table 1 as being powered *primarily* by recent star formation “S” or by an AGN “A”. Labels “(S)” and “(A)” indicate uncertain classifications. Note that these are *quantitative* classifications because both star formation and an AGN may contribute to the total radio luminosity a single galaxy.

Optical emission- and absorption-line spectra have often been used to classify galaxies as SFGs or AGNs. For example, Sadler et al. (2002) and Mauch & Sadler (2007) classified as AGNs all galaxies with absorption-line spectra like those of giant elliptical galaxies, absorption-line spectra with weak LINER-like emission lines, or stellar continua dominated by nebular emission lines stronger than Balmer emission lines; and they classified as SFGs all galaxies with spectra dominated by strong narrow H α and H β emission lines.

We decided not to use any optical indicators to determine the dominant radio energy sources in our galaxies. AGN signposts such as [O III] luminosity are often not correlated with radio luminosity (Best et al. 2005). We did not assume that star formation powers the radio sources in spiral galaxies or that AGNs drive radio emission from E and S0 galaxies. We did not use optical colors and fluxes, which may be biased by dust absorption. We did not use BPT (Baldwin et al. 1981) diagrams which plot the [O III]/H β ratio as a function of the [N II]/H α ratio because $\sim 40\%$ of nearby radio-loud AGN are too gas poor and optically inactive to be detected this way

Table 1
2MASX/NVSS catalog

2MASX J2000 name	$k_{20\text{fe}}$ (mag)	$d_{20\text{fe}}$ (")	$S_{1.4}$ (mJy)	Energy FIR	Source MIR	Type Final	cz (km s ⁻¹)	NED name
00000701+0816448	10.779	23.6	82.7	A	A	A	11602	UGC 12890
00001278+0107123	11.839	15.3	2.1	S	S	S	7390	CGCG 382-016
00002880+3246563	11.108	13.4	5.2	S	S	S	9803	IC 5373
00003138+2619318	11.967	13.2	7.5	S	S	S	7653	UGC 12896
00003564-0145472	11.488	16.1	2.8	?	S	(S)	7274	CGCG 382-017
00005234-3550370	11.548	15.2	48.4	A	A	A	15581	
00010444+0430001	12.013	15.4	2.7	S	S	S	8932	IC 5374
00011996+1306406	9.920	27.4	12.3	S	S	S	5366	NGC 7803
00013148+1120465	11.341	16.0	5.4	S	S	S	9099	IC 1526
00013359+0900445	11.234	15.0	2.7	?	S	(S)	9252	UGC 12912

Note. — Table 1 is published in its entirety in the electronic edition of the *Astrophysical Journal*. A portion is shown here for guidance regarding its form and content.

(Geréb et al. 2015). Thus our energy-source classification method is independent of the (Sadler et al. 2002) and (Mauch & Sadler 2007) classification method based on optical spectra.

Instead, we used only a combination of radio and infrared data to classify our radio sources. Radio sources powered by stars can be recognized because (1) > 99% obey the tight and nearly linear FIR/radio flux correlation (Condon et al. 1991), (2) they have the steep FIR spectral indices $\alpha(25\ \mu\text{m}, 60\ \mu\text{m}) < -1.5$ characteristic of cold dust emission (de Grijp et al. 1985), (3) they usually reside in galaxies having “dusty” MIR colors, and (4) they are roughly coextensive with their optical host galaxies. Radio sources powered by AGNs (1) are usually much stronger than expected from the FIR/radio correlation, (2) may be associated with warmer FIR sources, (3) usually reside in galaxies having the nearly blackbody MIR colors of “naked” stars, and (4) may contain jets and lobes extending well outside their host galaxies.

We used a combination of these four indicators as described in detail below to assign a primary energy source type to each 2MASX/NVSS galaxy in Table 1:

(1) The *IRAS* FIR/NVSS 1.4 GHz flux-density ratio was parameterized by the quantity

$$q \equiv \log \left[\frac{\text{FIR}/(3.75 \times 10^{12} \text{ Hz})}{S_{1.4 \text{ GHz}} (\text{W m}^{-2} \text{ Hz}^{-1})} \right], \quad (7)$$

where

$$\text{FIR} (\text{W m}^{-2}) \equiv 1.26 \times 10^{-14} [2.58 S_{60 \mu\text{m}} (\text{Jy}) + S_{100 \mu\text{m}} (\text{Jy})] \quad (8)$$

(Helou et al. 1988).

If a galaxy was detected by *IRAS* (*IRAS* flux quality code 2 or 3) at both 60 μm and 100 μm , the value of q was calculated directly from Equation 7. If a galaxy was detected at 60 μm but not detected (*IRAS* flux quality code 1) at 100 μm , an approximate q was estimated using the median observed $S_{100 \mu\text{m}} \sim 2S_{60 \mu\text{m}}$ (Yun et al. 2001). Conversely, if a galaxy was detected at 100 μm but not at 60 μm , q was estimated assuming $S_{60 \mu\text{m}} \sim S_{100 \mu\text{m}}/2$. If a galaxy was observed by *IRAS* but not detected at either 60 μm or 100 μm , an upper limit to q was calculated from the *IRAS* FSC 90%-completeness upper limits $S_{60 \mu\text{m}} < 0.36 \text{ Jy}$ and $S_{100 \mu\text{m}} < 1.2 \text{ Jy}$. Finally, if a

galaxy was in an area not adequately covered by *IRAS*, we set $q = ?$ and used only other classification methods.

The normalized probability distribution $P(q)$ of all galaxies in the complete 1.4 GHz flux-limited sample that were observed by *IRAS* is plotted as a histogram in Figure 4. Within that histogram the unshaded area indicates upper limits to q for galaxies observed but not detected by *IRAS* at either 60 μm or 100 μm , and the shaded area shows measured or estimated q values. Star-forming galaxies obeying the FIR/radio correlation are clustered in the narrow peak with mean $\langle q \rangle \approx 2.30$ and rms scatter $\sigma_q \approx 0.17$. The intrinsic scatter in q (Condon et al. 1991) is nearly equal to our measured σ_q , so the peak in Figure 4 has not been broadened significantly by flux-density measurement errors. Adding a dominant AGN to a $q = 2.3$ SFG would result in $q < 2.0$. To allow for the observed scatter in q , we classified galaxies with measured $q > 1.8$ as SFGs and galaxies with upper limits or measured values of $q < 1.8$ as primarily AGN-powered.

Galaxies with upper limits to q larger than 1.8 and galaxies not observed by *IRAS* could not be classified by this method. The NVSS and *IRAS* are comparably sensitive to SFGs: the value of q corresponding to the sensitivity limits $S_{1.4 \text{ GHz}} = 2.45 \text{ mJy}$, $S_{60 \mu\text{m}} = 0.36 \text{ Jy}$, and $S_{100 \mu\text{m}} = 1.2 \text{ Jy}$ is $q \approx 2.4$. Thus many galaxies not detected by *IRAS* do have upper limits to q larger than 1.8 (Figure 4).

(2) A FIR source warm enough to have

$$\alpha(25 \mu\text{m}, 60 \mu\text{m}) > -1.5 \quad (9)$$

indicates concentrated dust heating by a single AGN, rather than by a comparably luminous but more extended cluster of stars (de Grijp et al. 1985). The spectral-index error resulting from a 20% error in the 25 μm flux density is $\Delta\alpha(25 \mu\text{m}, 60 \mu\text{m}) \sim \pm 0.25$. To allow for spectral-index errors of sources with $\lambda = 25 \mu\text{m}$ signal-to-noise ratios as low as 5, we conservatively classified only galaxies with $\alpha(25 \mu\text{m}, 60 \mu\text{m}) > -1.25$ as primarily AGN-powered. There are 247 such “warm” galaxies, of which 77 also have $q < 1.8$ and the remaining 170 were newly classified as AGN-powered by their warm FIR spectra.

(3) *Wide-field Infrared Survey Explorer (WISE)* (Wright et al. 2010) MIR magnitudes in bands W1

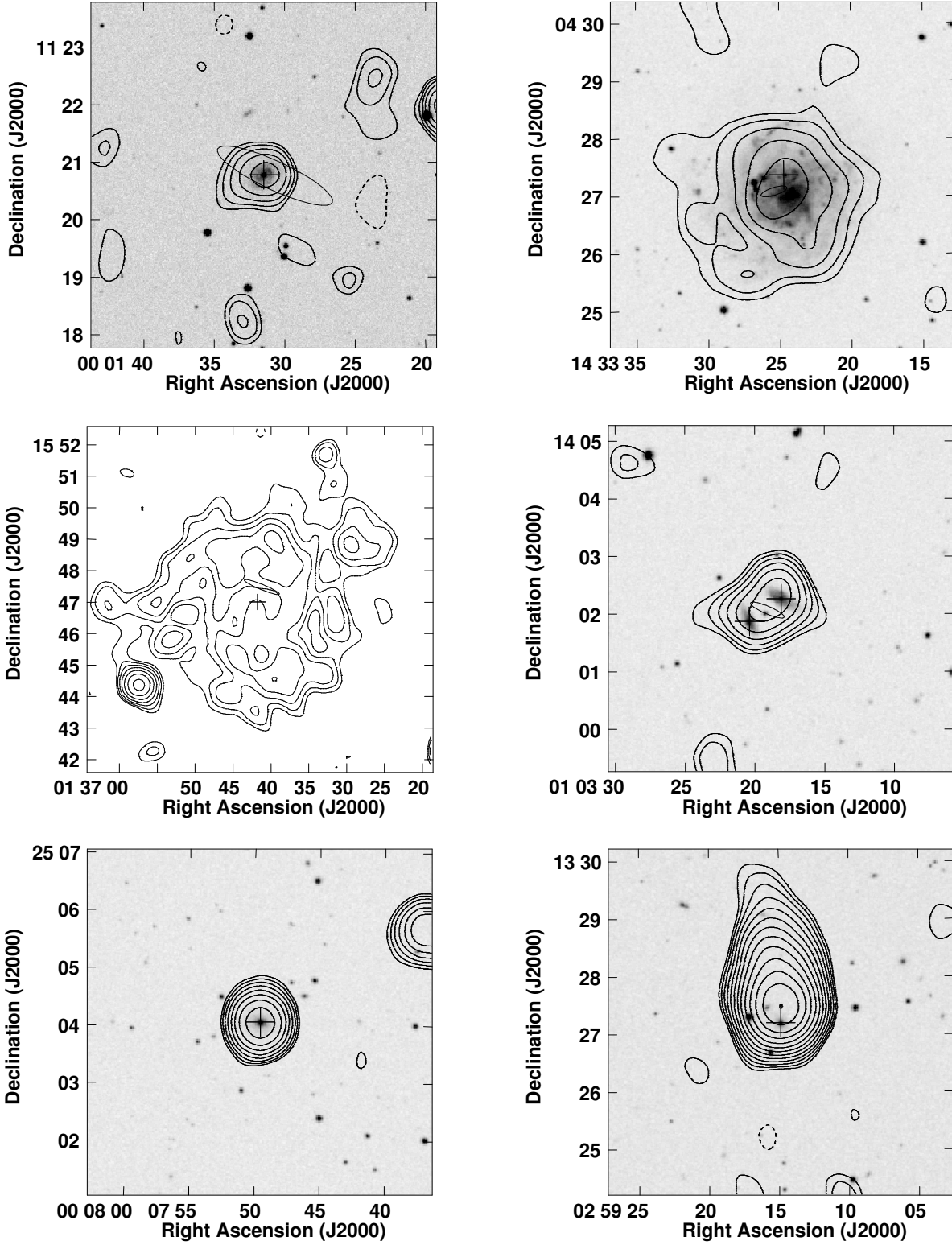


Figure 2. Selected finding charts. DSS gray-scale images are shown under NVSS contours plotted at $S_p = \pm 1 \text{ mJy beam}^{-1} \times 2^0, 2^{1/2}, 2^1, \dots$. 2MASX source positions are marked by crosses, ellipses outline *IRAS* position errors.

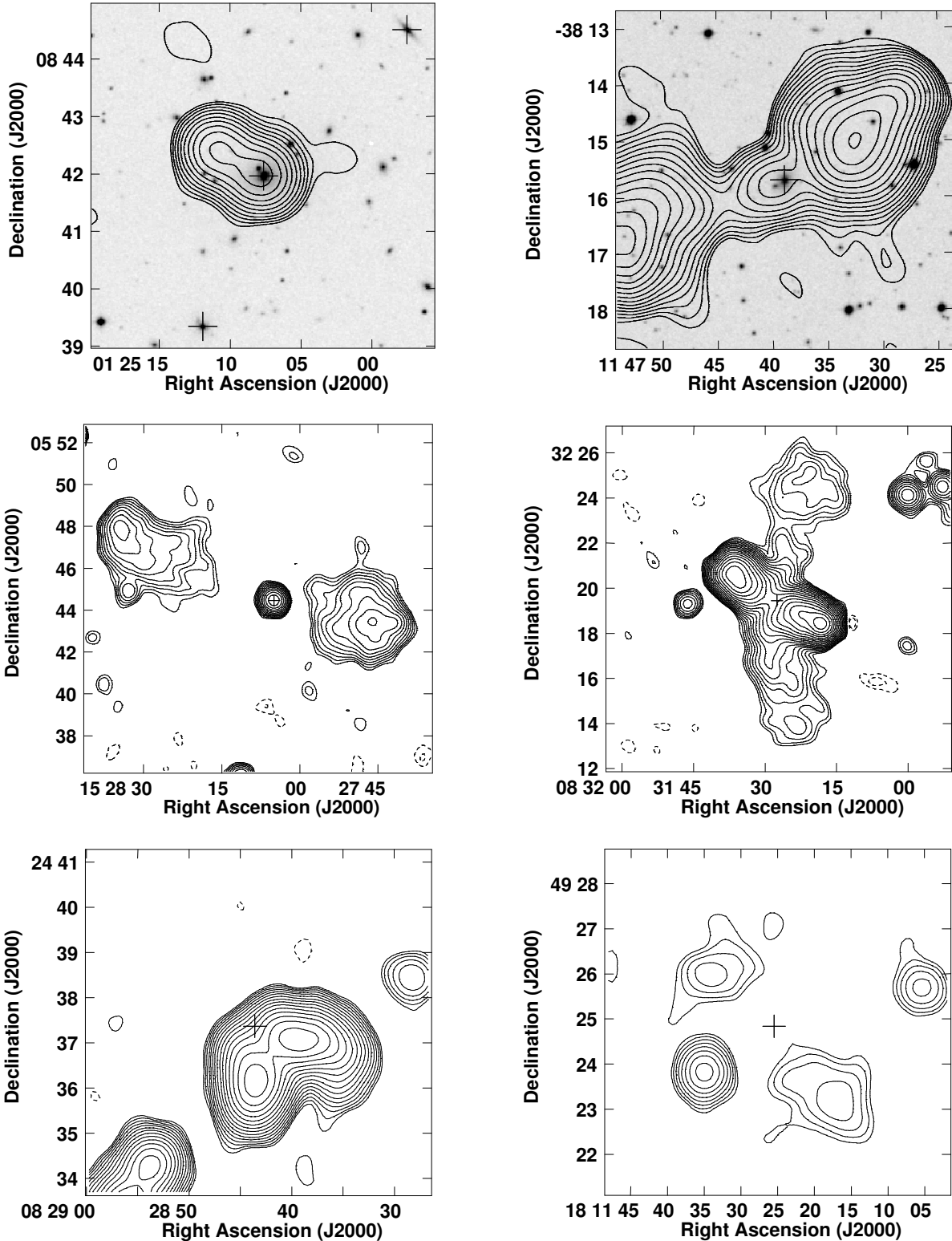


Figure 3. Additional selected finding charts. DSS gray-scale images are shown under NVSS contours plotted at $S_p = \pm 1 \text{ mJy beam}^{-1} \times 2^0, 2^{1/2}, 2^1, \dots$. 2MASX source positions are marked by crosses.

($\lambda = 3.4 \mu\text{m}$), W2 ($\lambda = 4.6 \mu\text{m}$), and W3 ($\lambda = 12 \mu\text{m}$) determine the colors ($W1 - W2$) and ($W2 - W3$) that help to distinguish AGNs residing in elliptical galaxies and Seyfert galaxies from dusty spiral galaxies dominated by ongoing star formation, as illustrated in Fig-

ure 5. Stars alone and dustless elliptical galaxies (lower left circle in Figure 5) have low values of ($W1 - W2$) and ($W2 - W3$) because the W1, W2, and W3 wavelengths are on the Rayleigh-Jeans side of the blackbody peak of most stars, and the limiting Rayleigh-Jeans spectral

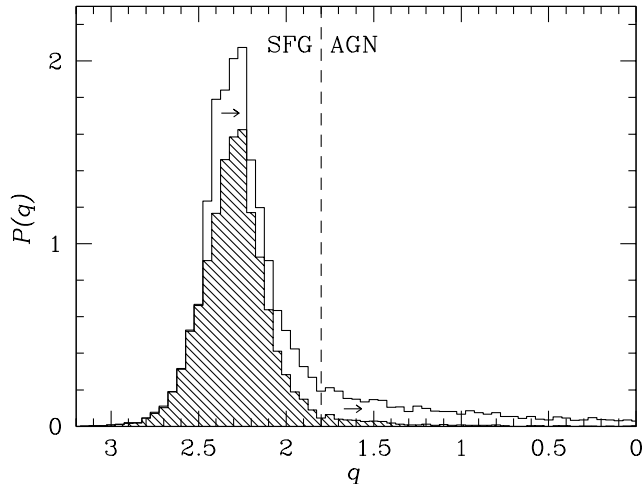


Figure 4. For 2MASX/NVSS galaxies with $S_{1.4 \text{ GHz}} \geq 2.45 \text{ mJy}$, the normalized probability distribution of the measured FIR/radio ratio q is shown by the shaded histogram and upper limits for those observed but not detected by *IRAS* are indicated by the unshaded part of the histogram. The vertical dashed line separates SFGs with measured $q > 1.8$ from AGNs with upper limits or measured $q < 1.8$. Abscissa: FIR/radio flux ratio q (Equation 7). Ordinate: Probability density $P(q)$.

index $\alpha = +2$ corresponds to $(W1 - W2) \approx -0.05$ and $(W2 - W3) \approx -0.07$ for the *WISE* flux-density scales and frequencies listed in Table 1 of Jarrett et al. (2011). The sublimation temperature of large interstellar dust grains is too low for them to affect $(W1 - W2)$ significantly, but dust in SFGs increases $(W2 - W3)$. Nuclear emission from Seyfert galaxies (upper right circle in Figure 5) can increase $(W1 - W2)$ enough to separate AGNs from SFGs. Thus radio sources in galaxies above the broken line specified by

$$W1 - W2 = +0.8 \quad (W2 - W3 \geq 3.1) \quad (10)$$

$$W1 - W2 = (W2 - W3 - 1.82)/1.6 \quad (W2 - W3 < 3.1)$$

are probably AGN-powered, and those below the line are likely powered by ongoing star formation. Although the *WISE* MIR colors are less reliable indicators than the *IRAS* FIR/radio correlation, they are available for nearly all 2MASX/NVSS galaxies, so we used them to classify cases that have neither measured q values nor upper limits $q < 1.8$.

WISE does not have the far-infrared coverage needed to yield q (Equation 7), but the $\lambda = 22 \mu\text{m}$ *WISE* magnitude $W4$ can be used to define a similar quantity

$$q_{22} \equiv \log[S(22 \mu\text{m})/S(1.4 \text{ GHz})], \quad (11)$$

where

$$\log \left[\frac{S(22 \mu\text{m})}{\text{Jy}} \right] = 0.918 - 0.4 W4 \quad (12)$$

(Jarrett et al. 2011). The normalized probability distribution $P(q_{22})$ is shown in Figure 6 for all 2MASX/NVSS galaxies with $k_{20\text{fe}} \leq 12.25$ and $S(1.4 \text{ GHz}) \geq 2.45 \text{ mJy}$ (black histogram). Galaxies with *WISE* MIR colors below the broken line in Figure 5 (*WISE* energy source S) are represented by the blue histogram, and galaxies above the broken line in Figure 5 (*WISE* energy source A) by the red histogram. Like the distribution of q in

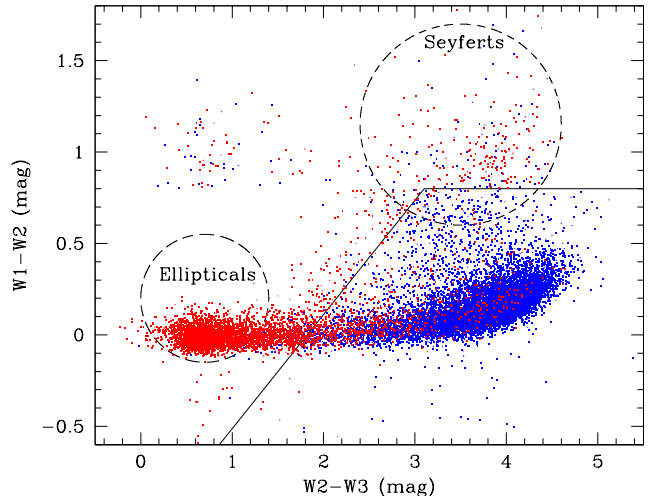


Figure 5. The mid-infrared colors $(W1 - W2)$ ($[3.4 \mu\text{m}] - [4.6 \mu\text{m}]$) and $(W2 - W3)$ ($[4.6 \mu\text{m}] - [12 \mu\text{m}]$) can be used to separate galactic stars and elliptical galaxies (lower left dashed circle) from Seyfert galaxies (upper right dashed circle) and from dusty spiral galaxies with ongoing star formation (below the broken line), as shown in Wright et al. (2010) Figure 12. Galaxies listed as A or (A) in Table 1 are shown as red points; S or (S) galaxies are blue. Abscissa: $(W2 - W3)$ (mag). Ordinate: $(W1 - W2)$ (mag).

Figure 4, the distribution of q_{22} in Figure 6 has a narrow peak dominated by SFGs and a long tail of galaxies containing radio-loud AGNs. Thus *WISE* MIR colors and *WISE* MIR/radio flux ratio parameters q_{22} provide independent energy-type classifications that largely agree.

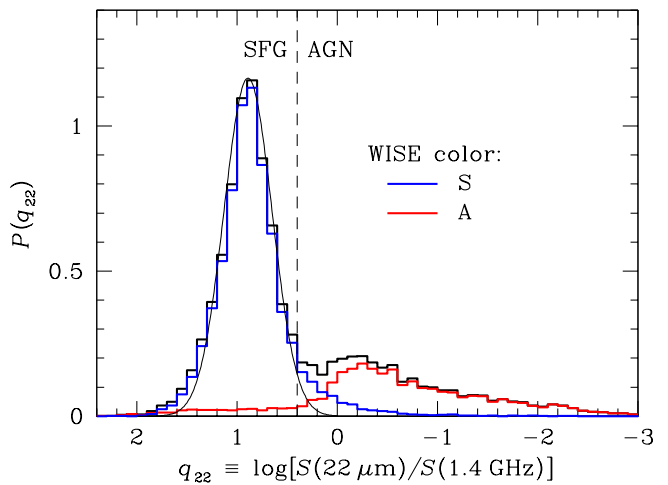


Figure 6. The normalized probability distribution $P(q_{22})$ of $q_{22} \equiv \log[S(22 \mu\text{m})/S(1.4 \text{ GHz})]$ for all 2MASX/NVSS galaxies with $S(1.4 \text{ GHz}) \geq 2.45 \text{ mJy}$ is indicated by the black histogram. The blue and red histograms show the galaxies classified as S or A by their *WISE* MIR colors (Equation 10 and Figure 5). The vertical dashed line at $q_{22} = +0.4$ separates most SFGs ($q_{22} > +0.4$) from most AGNs ($q_{22} < +0.4$). The Gaussian fit to the narrow peak has mean $\langle q_{22} \rangle = 0.89$ and rms width $\sigma = 0.24$. Abscissa: *WISE* MIR/radio flux-ratio parameter q_{22} . Ordinate: Probability density $P(q_{22})$.

The main advantage of the *WISE* q_{22} distribution over the *IRAS* q distribution is that all but a handful of 2MASX/NVSS galaxies were detected by *WISE* at

$\lambda = 22 \mu\text{m}$. The drawback of q_{22} is contamination of $S(22 \mu\text{m})$ by emission from warm dust heated by AGNs, making it a somewhat less reliable parameter than q for distinguishing SFGs from AGNs. For our final MIR classifications, we used the *WISE* color criterion (Equation 10). We used q_{22} only for a few galaxies having no *IRAS* data, as described in items 3. through 5. in the list at the end of Subsection 4.1.

(4) Radio morphology complements the three photometric indicators above. Radio sources powered by star formation are roughly coextensive with the star-forming regions, their synchrotron emission broadened only slightly by diffusion of cosmic-ray electrons (Murphy et al. 2008). Coextensive synchrotron emission and free-free absorption by ionized hydrogen at electron temperature $T_e \sim 10^4$ K limits the 1.4 GHz brightness temperature of SFGs to $T_b \lesssim 10^5$ K (Condon 1992). AGNs can produce radio jets and lobes that extend well outside their host galaxies, and they can produce compact radio cores with brightness temperatures $T_b \gg 10^5$ K.

To identify very extended radio jets and lobes, we inspected the finding charts of all galaxies having two or more NVSS components. Most are either elliptical galaxies or spiral galaxies larger than the radio sources and much larger than the $\theta = 45''$ FWHM NVSS beam.

The only spiral galaxy with radio emission outside the galaxy of stars is the Seyfert NGC 4258 (2MASX J12185761+4718133) with unique “anomalous radio arms” (van der Kruit et al. 1972). NGC 4258 was not covered by the *IRAS* FSC, but we classified its radio source as primarily AGN-powered on the basis of *WISE* photometry ($q_{22} = -0.10$).

All but one of the multicomponent NVSS sources not identified with large spiral galaxies are so radio-loud (either $q < 1.8$ or $q_{22} < 0.4$) that they had already been photometrically classified as AGN-powered. The sole exception is luminous triple radio source in 2MASX J23415138–3729306, which has neither *IRAS* nor *WISE* photometry and was classified as AGN-powered on the basis of radio morphology alone.

Sub-arcsecond resolution is needed to resolve sources brighter than $T_b \sim 10^5$ K, so the NVSS alone is unable to distinguish AGN cores from compact SFGs.

The four indicators above do not always agree, so the final energy source types A, (A), S, and (S) listed in Table 1 were derived by reconciling the various *IRAS* and *WISE* classifications as follows:

1. If *IRAS* and *WISE* agree on A or S, the final classification is A or S.
2. if *IRAS* and *WISE* disagree on A or S, the *IRAS* result was kept but qualified as uncertain (A) or (S).
3. If *IRAS* = ? (no *IRAS* data) and $q_{22} < 0.4$ (radio loud), then the final classification is M if the *WISE* MIR color classification = ? and (M) if it = S.
4. If *IRAS* = ?, $0.7 > q_{22} \geq 0.4$, and *WISE* = S, then the final classification is (S).
5. If *IRAS* = ?, $q_{22} \geq 0.7$, and *WISE* = S, then the final classification is S.

Table 2
Source classification matrix

	A	(A)	S	(S)
Aa	644	32	6	8
Aa?	27	5	1	5
Aae	101	18	27	15
Aae?	24	10	27	10
Ae	41	28	19	16
Ae?	10	17	23	5
SF	17	48	2018	103
SF?	3	12	64	18
?	21	5	33	5

Among our 15,043 galaxies classified by radio and infrared criteria are 3,466 that had been classified by Mauch & Sadler (2007) on the basis of optical line spectra. Their star-forming galaxies were labeled SF, and their AGNs were divided into three subtypes: Aa (pure absorption-line spectra like those of giant elliptical galaxies), Aae (spectra with absorption lines and weak narrow LINER-like emission lines), or Ae (conventional Type II AGN spectra with nebular emission lines such as [OII], [OIII], or [NII] that are stronger than any hydrogen Balmer emission lines, or conventional Type I AGN spectra with strong and broad hydrogen Balmer emission lines). Uncertain optical classifications were indicated by ‘?’.

Table 2 compares our independent galaxy classification methods for these 3,466 galaxies, and the agreement is better than we had expected. Of the 888 galaxies we classified as A, Mauch & Sadler (2007) classified 867, 847 (97.7%) as various AGN types and only 20 (2.3%) as SF or SF?. We classified 2218 galaxies as S and Mauch & Sadler (2007) classified 2185 of them, 2082 (95.3%) as SF or SF? and 103 (4.7%) as various AGN types. Of their 2186 SF galaxies, we classified 2121 (97.0%) as S or (S), 17 (0.8%) as A, and 48 (2.2%) as (A). They classified 690 galaxies as Aa; we classified 676 (98.0%) as A or (A) and 14 (2.0%) as S or (S). The agreement is lower for the 161 Aae galaxies (74%) and the 104 Ae galaxies (66%). Most of these are star-forming LINERs or Seyfert II galaxies whose AGN radio luminosities appear to be less than half their total radio luminosities.

4.2. 1.4 GHz Nearby Galaxy Counts

The differential source count $n(S)dS$ is the number of sources per steradian with flux densities between S and $S+dS$. The differential contribution dT_b of radio sources between S and $S+d \log(S)$ to the Rayleigh-Jeans sky brightness temperature T_b is

$$\frac{dT_b}{d \log(S)} = S^2 n(S) \left[\frac{\ln(10)c^2}{2k_B \nu^2} \right], \quad (13)$$

where $k_B \approx 1.38 \times 10^{-23} \text{ J K}^{-1}$ is the Boltzmann constant. Figure 7 is a logarithmic plot comparing the brightness-weighted 1.4 GHz counts $S^2 n(S)$ for all extragalactic sources (Condon 1984) (upper solid curve), all 2MASX/NVSS sources with $k_{20\text{Fe}} \leq 12.25$ and $S_{1.4 \text{ GHz}} \geq 2.45 \text{ mJy}$ (lower solid curve), 2MASX/NVSS sources powered primarily by star formation (open circles), and 2MASX/NVSS sources powered by AGNs (filled circles). Below $S \approx 0.1 \text{ Jy}$ the nearby ($z \lesssim 0.1$) 2MASX/NVSS sources contribute $\lesssim 1\%$ of the total

radio-source background.

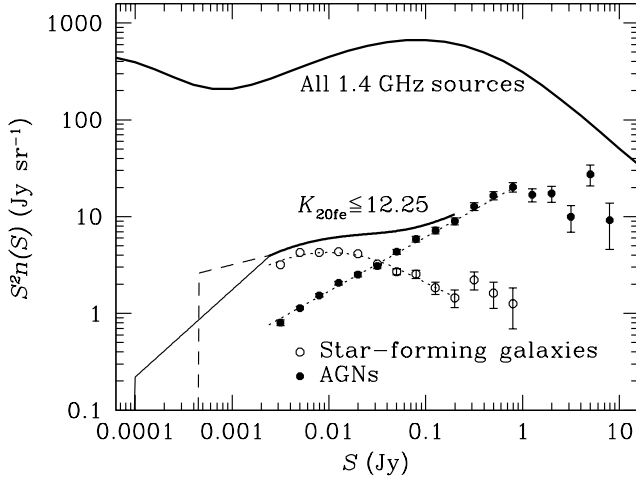


Figure 7. The brightness-weighted 1.4 GHz differential counts $S^2 n(S)$ are plotted separately for all radio sources (Condon 1984) (solid curve) and for 2MASX/NVSS galaxies brighter than $k_{20fe} = 12.25$ whose radio sources are powered by stars (open circles) or AGNs (filled circles). $S^2 n(S)$ is proportional to the contribution per decade of flux density to the 1.4 GHz sky brightness temperature. The light straight line matching the $P(S_p)$ distribution (Figure 8) suggests that most galaxies with $k_{20fe} \leq 12.25$ have 1.4 GHz flux densities $S \gtrsim 0.1$ mJy. Abscissa: 1.4 GHz flux density S (Jy). Ordinate: Brightness-weighted differential count $S^2 n(S)$ (Jy sr^{-1}).

The 2MASX catalog is quite complete for $k_{20fe} \leq 12.25$ and bright 2MASX galaxies have a nearly static Euclidean source count $n(S) \propto S^{-5/2}$ (Jarrett 2004). Radio sources powered by star formation typically have relatively low absolute spectral luminosities $L \sim 10^{22} \text{ W Hz}^{-1}$ (Condon et al. 2002) yielding flux densities $S \sim 0.01$ Jy at the distances $d \sim 100$ Mpc ($cz \sim 7,000 \text{ km s}^{-1}$) typical of 2MASX/NVSS SFGs. At flux densities $S > 0.01$ Jy the volume accessible to the 2MASX/NVSS sample of SFGs is almost completely IR-limited, so their radio source count should also be nearly Euclidean: $S^2 n(S) \propto S^{-1/2}$ as suggested by the dotted line connecting the open points in Figure 7. At lower flux densities the 2MASX/NVSS sample depth becomes more radio-limited, so the contribution by SFGs to $S^2 n(S)$ flattens out and eventually turns over. Nearby 2MASX/NVSS radio AGNs are typically more luminous than SFGs by factors of $\sim 10^{2.5}$ (Condon et al. 2002), so their source count is IR-limited and nearly Euclidean only for the small number of AGNs stronger than $S \sim 1$ Jy. Nearly all 2MASX/NVSS AGNs are much weaker and the volume sampled is strongly limited by the radio sensitivity limit. The dotted straight line fitted to the AGN count (filled circles) in Figure 7 has a slope $d \log[S^2 n(S)]/d \log(S) \approx +0.6$ for $S \ll 1$ Jy. This slope is close to the slope $\alpha \approx +0.5$ of the 1.4 GHz spectral power density function $U_{dex}(L)$ at spectral luminosities $L \ll 10^{24} \text{ W Hz}^{-1}$ (see Section 7.2).

Only 15,043 of the 55,288 (27%) 2MASX galaxies brighter than $k_{20fe} = 12.25$ contain NVSS sources stronger than 2.45 mJy at 1.4 GHz. However, the nor-

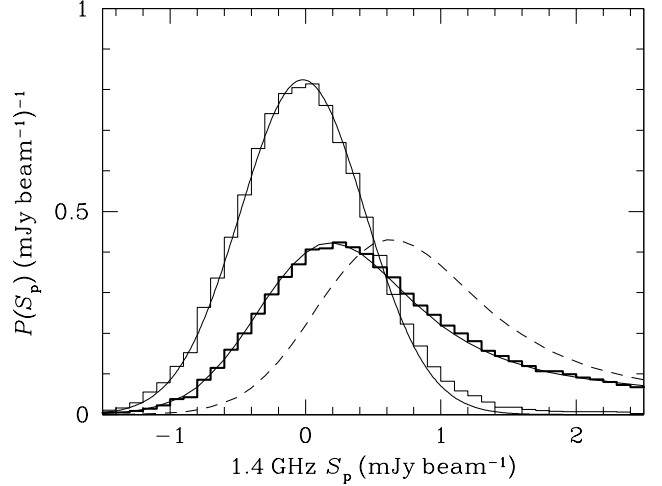


Figure 8. The distribution of NVSS peak flux densities S_p at the positions of all 2MASX sample galaxies is plotted as the heavy histogram, and the light histogram shows the corresponding peak flux densities at “blank” positions offset 1° to the north. The source count indicated by the light solid line in Figure 7 yields the best fits (solid curves) to these histograms. The dashed curve that doesn’t fit the data is the $P(S_p)$ distribution corresponding to the dashed source count in Figure 7.

malized probability distribution $P(S_p)$ of NVSS peak flux densities S_p at the positions of all 55,288 2MASX sample galaxies (heavy histogram in Figure 8) constrains the radio source count well below 2.45 mJy. The light histogram shows the matching distribution of peak flux densities at “blank” positions offset 1° to the north. It is well fit by a noise Gaussian with rms width $\sigma = 0.47 \text{ mJy beam}^{-1}$ (light curve) plus a thin positive-going tail produced by background radio sources. The NVSS on-source distribution is the convolution of the off-source distribution and the peak flux density distribution of 2MASX galaxies. To the extent that most weak 2MASX radio sources are unresolved in the $\theta = 45''$ FWHM NVSS beam, $S_p \approx S$ and

$$\Omega n(S) dS = N P(S_p) dS_p. \quad (14)$$

For any $S^2 n(S)$ (Figure 7) we can solve for

$$P(S_p) = \left(\frac{\Omega}{N S^2} \right) S^2 n(S). \quad (15)$$

To the degree that the weighted differential count can be approximated by a power law $S^2 n(S) \approx k S^\gamma$ over the flux-density range S_1 to S_2 , the number of sources ΔN with flux densities between S_1 and S_2 is

$$\Delta N \approx \Omega \int_{S_1}^{S_2} k S^{\gamma-2} dS = \left(\frac{\Omega k}{1-\gamma} \right) (S_1^{\gamma-1} - S_2^{\gamma-1}). \quad (16)$$

Among the $N = 55,288$ 2MASX galaxies brighter than $k_{20fe} = 12.25$ in $\Omega = 7.016 \text{ sr}$, there are $\Delta N = 40,245$ with peak flux densities $S_2 < 2.45$ mJy.

Equation 16 is an integral constraint on S_1 (there can’t be more 2MASX/NVSS radio sources than 2MASX galaxies) as a function of the other two source-count variables k and γ . Continuity of the direct source count $S^2 n(S) \approx 4 \text{ sr}^{-1}$ at $S \approx 0.003$ Jy (Figure 7) fixes k for any γ . The best value of the remaining unknown

γ is the one that yields the best fit to the heavy $P(S_p)$ histogram in Figure 8. For example, the power-law extrapolation $S^2 n(S) = 17.9S^{0.25}$ of the direct count of 2MASX galaxies with $k_{20\text{fe}} \leq 12.25$ above $S = 2.45$ mJy yields the dashed line in Figure 7 that must break at $S_1 \approx 0.46$ mJy lest the number of radio sources exceed the number of galaxies. However, this solution is unsatisfactory because it predicts the dashed $P(S_p)$ distribution in Figure 8 that is shifted far to the right of the observed distribution (heavy histogram).

The best power-law fit is $S^2 n(S) \approx 880S^{-0.90}$ cutting off at $S_1 \approx 0.0001$ Jy, as shown by the light straight line in Figure 7 and the continuous curve that is a good match to the heavy histogram in Figure 8. We conclude that (1) the brightness-weighted count of nearby sources fainter than 2.45 mJy must converge rapidly, and (2) the NVSS is sufficiently sensitive to have detected individually those sources that contribute most of the low redshift ($z \lesssim 0.05$) sky brightness. It also appears that most 2MASX galaxies brighter than $k_{20\text{fe}} = 12.25$ are radio sources stronger than $S \sim 0.1$ mJy and should be detectable above the planned $S_p \approx 0.05$ mJy sensitivity limit of the upcoming EMU survey (Norris et al. 2011).

5. THE SPECTROSCOPICALLY COMPLETE SUBSAMPLE

All but 7 of the 9,517 2MASX/NVSS galaxies with $k_{20\text{fe}} \leq 11.75$ have published spectroscopic velocities cz or new velocities reported in Appendix B.

To estimate accurate distances from the observed heliocentric velocities, we first converted the heliocentric velocities $v \equiv cz$ to velocities v_{CMB} in the frame of the cosmic microwave background (CMB) using

$$v_{\text{CMB}} = v + v_{\text{apex}} [\sin(b) \sin(b_{\text{apex}}) + \cos(b) \cos(b_{\text{apex}}) \cos(l - l_{\text{apex}})], \quad (17)$$

where $(l_{\text{apex}}, b_{\text{apex}}) = (264.14^\circ, 48.26^\circ)$ and $v_{\text{apex}} = 371.0 \text{ km s}^{-1}$ (Fixsen et al. 1996).

Large-scale structures (e.g., galaxy clusters) cause additional deviations from the local Hubble flow that depend on position and redshift. We adopted the local bulk flow models of Carrick et al. (2015) to correct for this effect.

The Carrick et al. (2015) model of the peculiar velocity field is given as a 257^3 voxel cube in right-handed galactic Cartesian coordinates with i, j , and k indices corresponding to galactic X, Y, Z in Mpc h^{-1} , with the i index running fastest. The voxel centers run from $-200h^{-1}$ to $200h^{-1}$ Mpc so the voxel spacing is $1.5625h^{-1}$ Mpc. The i, j, k indices can be converted to Cartesian galactic coordinates using

$$X = (i - 128) \times 400./256. \quad (18)$$

$$Y = (j - 128) \times 400./256. \quad (19)$$

$$Z = (k - 128) \times 400./256. \quad (20)$$

The center of the cube $[128, 128, 128]$ represents the Local Group. All peculiar velocities v_{pec} in the cube are relative to the CMB and are generated by the galaxy density models of Carrick et al. (2015), which depend upon the cosmological density of matter Ω_m (taken to be 0.3 in this study) and the bias b^* of an L^* galaxy. Along the radial line to each galaxy, we solved

$$H_0 r + v_{\text{pec}}(r) = v_{\text{CMB}} \quad (21)$$

to obtain the corrected galaxy velocity $v_c = cz_c$.

The histograms in Figure 9 show the normalized probability distributions $P(cz)$ of corrected velocities cz_c for galaxies whose radio sources are powered by stars (unshaded area) or by AGNs (shaded). Star-forming galaxies outnumber AGNs by a ratio of $>2:1$ in this sample of bright galaxies, especially at lower redshifts. The median velocity of star-forming galaxies is only $\langle cz_c \rangle \approx 0.6 \times 10^4 \text{ km s}^{-1}$, about half the median velocity $\langle cz_c \rangle \approx 1.2 \times 10^4 \text{ km s}^{-1}$ of galaxies with AGN-powered radio sources.

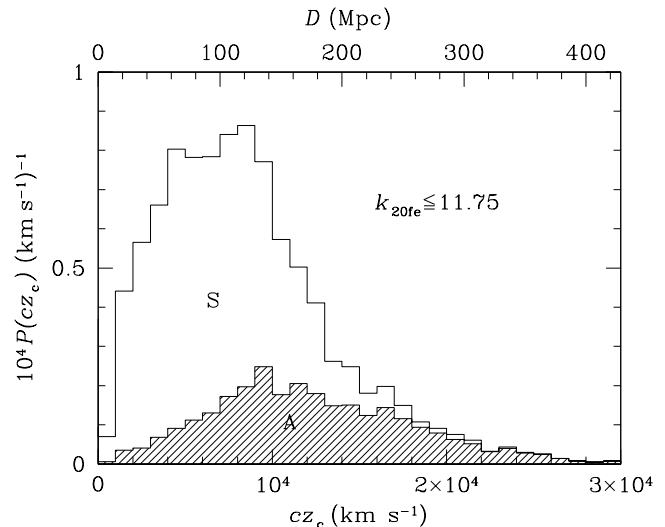


Figure 9. All but 7 of the 9,517 2MASX/NVSS galaxies with $k_{20\text{fe}} \leq 11.75$ have spectroscopic redshifts. Histograms of their corrected velocities cz_c are shown separately for galaxies whose radio sources are powered by AGNs (A) or by stars (S). The corresponding Hubble distances for $H_0 = 70 \text{ km s}^{-1} \text{ Mpc}^{-1}$ are also shown. Lower Abscissa: cz_c (km s^{-1}). Upper Abscissa: Hubble distance D (Mpc) Ordinate: $10^4 P(cz_c)$ (km s^{-1}) $^{-1}$.

6. LOCAL 1.4 GHz LUMINOSITY FUNCTIONS

The local luminosity function specifies the mean space density of galaxies in the nearby universe as a function of spectral luminosity. The universe is evolving and homogeneous on large scales, so the local luminosity function more usefully represents the universal average space density during the present epoch rather than our particular location in space. We derived separate 1.4 GHz luminosity functions for radio sources powered by star formation and by AGNs. They are today's benchmarks for comparing with higher-redshift samples to constrain models for the cosmological evolution of star formation and AGN activity.

The 2MASX/NVSS spectroscopic subsample should yield reliable 1.4 GHz luminosity functions because redshifts are available for nearly all galaxies and it is complete for galaxies that are brighter than $k_{20\text{fe}} = 11.75$ at $\lambda = 2.16 \mu\text{m}$, stronger than $S = 2.45$ mJy at 1.4 GHz, and lie in the solid angle $\Omega = 7.016 \text{ sr}$ defined by $\text{J2000 } \delta > -40^\circ$ and $|b| > 20^\circ$. The 2MASX catalog itself is actually complete and reliable for galaxies much fainter than $k_{20\text{fe}} = 11.75$; our magnitude limit reflects the availability of spectroscopic redshifts. The NVSS

sample includes all sources with catalog flux densities $S \geq 2.5$ mJy. However, the NVSS catalog flux densities are rounded to the nearest 0.1 mJy, so sources as faint as $S = 2.45$ mJy are listed as having $S = 2.5$ mJy in the catalog. The spectroscopic redshifts are from Huchra et al. (2012) or from new optical and NIR spectra obtained with the Apache Point Observatory (APO) 3.5 m telescope, as described in Appendix B.

The 1.4 GHz spectral luminosity function $\rho(L) dL$ is defined as the space density of sources with 1.4 GHz spectral luminosities between L and $L + dL$. The range of spectral luminosities spanned by galaxies is so large that it is convenient to define a logarithmic spectral luminosity function

$$\rho_{\text{dex}}(L) \equiv \rho(L) \frac{dL}{d \log(L)} = \ln(10) L \rho(L) \quad (22)$$

specifying the space density of sources per decade of spectral luminosity.

The 1.4 GHz spectral luminosity of each source is

$$L = 4\pi D_L^2 S_{1.4} (1+z)^{-(1+\alpha)}, \quad (23)$$

where $D_L = (1+z)D_C$ is the luminosity distance to the radio source, D_C is the comoving distance, $S_{1.4}$ is the 1.4 GHz NVSS flux density, and $\alpha = -0.7$ is the mean spectral index ($S \propto \nu^\alpha$) of sources selected at 1.4 GHz (Condon 1984). The absolute magnitude $K_{20\text{fe}}$ was calculated using

$$K_{20\text{fe}} = k_{20\text{fe}} - 5 \log\left(\frac{D_L}{10 \text{ pc}}\right) - k(z), \quad (24)$$

where $k(z) = -6.0 \log(1+z)$ is the k -correction that is independent of galaxy type and valid for all $z \leq 0.25$ (Kochanek et al. 2001). We therefore used $z_{\text{max}} = 0.25$ as the maximum possible redshift when calculating V_{max} values for our galaxy sample.

6.1. Maximum Redshifts

We plotted the maximum redshifts z_{max} at which galaxies could remain in our spectroscopic subsample as functions of both 1.4 GHz spectral luminosity (Figure 10) and $\lambda = 2.16 \mu\text{m}$ absolute magnitude $K_{20\text{fe}}$ (Figure 11). Star-forming galaxies (blue triangles) span the majority of the redshift range ($0.0017 \lesssim z \lesssim 0.12$) and absolute magnitudes ($-18 \gtrsim K_{20\text{fe}} \gtrsim -27$), but are mainly limited to 1.4 GHz luminosities $\log[L(\text{W Hz}^{-1})] \lesssim 23$. AGNs (black circles) dominate both the high radio luminosities and absolute magnitudes $K_{20\text{fe}}$, but are fewer in number at the lowest redshifts ($z \lesssim 0.007$).

6.2. Correction for Local Overdensity

Galaxies cluster and we are located in a galaxy, so the space density ρ_P of the nearest galaxies is somewhat greater than the mean density ρ of all galaxies. We corrected our local luminosity function for the local overdensity within a distance r using the equation (Fisher et al. 1994)

$$\frac{\rho_P}{\rho} = 1 + \frac{3}{3-\gamma} \left(\frac{r_0}{r}\right)^\gamma. \quad (25)$$

The correlation function parameters of *IRAS* galaxies are appropriate for describing the clustering of the

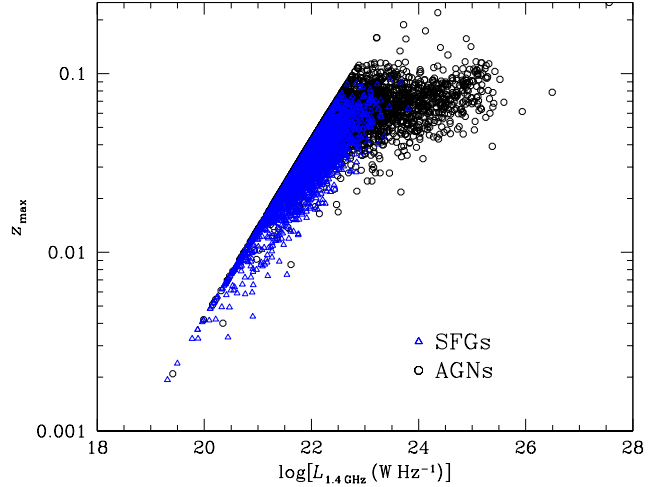


Figure 10. Maximum redshifts out to which a 2MASX/NVSS source could be moved and remain in the spectroscopic subsample, as a function of 1.4 GHz luminosity. The maximum redshifts for star-forming galaxies (blue triangles) and AGNs (black circles) are shown as a function of 1.4 GHz radio luminosity.

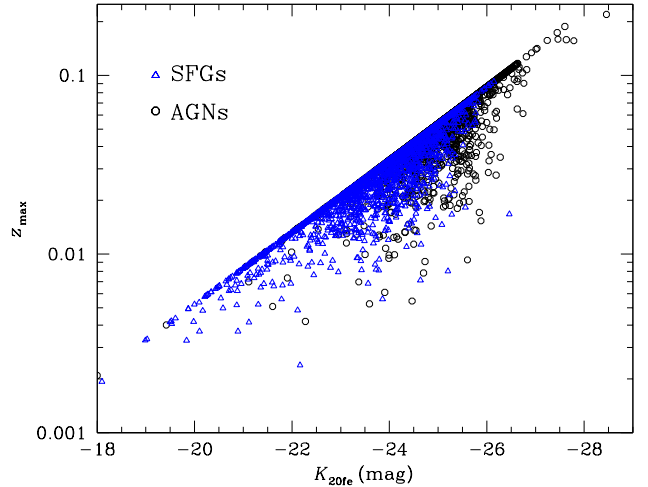


Figure 11. Maximum redshifts out to which a 2MASX/NVSS source could be moved and remain in the spectroscopic subsample, as a function of $K_{20\text{fe}}$. The maximum redshifts for star-forming galaxies (blue triangles) and AGNs (black circles) are shown as a function of $K_{20\text{fe}}$.

2MASX/NVSS galaxies; they are $r_0 = 3.76 h^{-1}$ and $\gamma = 1.66$ for $r < 20 h^{-1}$ Mpc (Fisher et al. 1994). For $r < 20 h^{-1}$ Mpc, the volume within r was multiplied by ρ_P/ρ in our calculation of V_{max} ; otherwise the volume was left unchanged. To minimize uncertainties introduced by large values of this correction for local-group galaxies, we excluded 48 galaxies in the volume with $r < 5$ Mpc (corrected $cz_c < 350 \text{ km s}^{-1}$, or $z \lesssim 0.0017$) when calculating luminosity functions. Only about 5% of our sample galaxies have $r < 20 h^{-1}$ Mpc ≈ 29 Mpc, so correcting for the local overdensity has only a small effect on our radio luminosity functions.

6.3. The Distribution of V/V_{max}

If the radio sources are randomly distributed throughout the corrected volume, the distribution of V/V_{max} should be uniform in the interval $[0,1]$ and have a mean $\langle V/V_{\text{max}} \rangle \approx 0.5$. The standard deviation of a uni-

form distribution on the interval $[0,1]$ is $12^{-1/2}$, so the rms uncertainty in $\langle V/V_{\max} \rangle$ of $N \gg 1$ radio sources is $\sigma \approx (12N)^{-1/2}$. A statistically significant departure from a uniform distribution with mean 0.5 may indicate one or more of the following: poor corrections for the local overdensity, incorrect sample limits, strong clustering, or monotonic evolution of sources during the lookback times spanned by the sample volume. For the 2MASX/NVSS galaxies used to determine the local luminosity function, the 6699 star-forming galaxies have $\langle V/V_{\max} \rangle = 0.500 \pm 0.004$, the 2763 AGNs have $\langle V/V_{\max} \rangle = 0.494 \pm 0.005$, and all 9462 galaxies have $\langle V/V_{\max} \rangle = 0.497 \pm 0.003$. Thus our $\langle V/V_{\max} \rangle$ test detects no monotonic evolution during the sample-limited lookback time $\tau \sim 1 - 2$ Gyr.

The normalized probability densities of V/V_{\max} in 20 bins of width $\Delta(V/V_{\max}) = 0.05$ are plotted separately for star-forming galaxies and AGNs in Figure 12. The V/V_{\max} distribution for AGNs closely follows a uniform distribution with a $\chi^2_\nu \approx 1.08$. In contrast, the distribution for star-forming galaxies appears to deviate slightly, with a $\chi^2_\nu \approx 2.04$, marginally significant at the ~ 0.01 level. This slight deviation from a uniform distribution can be mostly attributed to the peak in the bin of V/V_{\max} from 0.80–0.85. This is caused mainly by galaxies whose z_{\max} is limited by radio luminosity rather than K band magnitude. This peak would be a marginally statistically significant 3.6σ bump for the star-forming galaxies if galaxies were distributed randomly in space. However, our V/V_{\max} fluctuations are consistent with the statistical fluctuations expected in clustered galaxy samples mildly exacerbated by the NVSS catalog flux-density quantization.

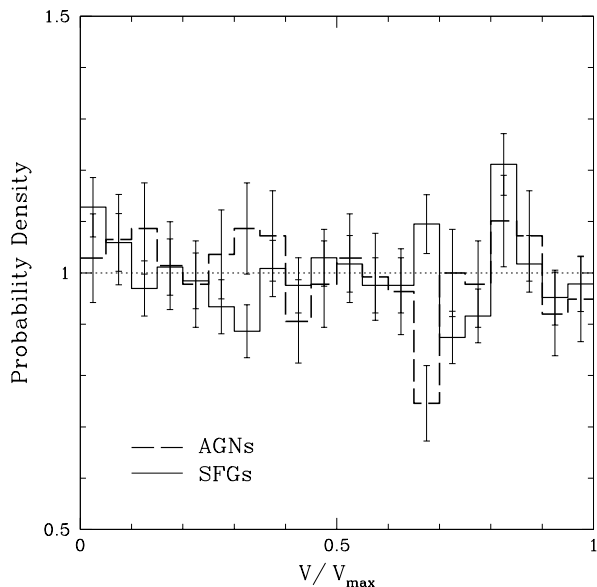


Figure 12. Binned distributions of V/V_{\max} for star-forming galaxies (solid line) and AGNs (dashed line) with the rms uncertainties expected for randomly distributed galaxies. Abscissa: V/V_{\max} . Ordinate: Binned probability density.

6.4. Luminosity Function Results

We sorted our galaxies into luminosity bins of width $\Delta \log(L) = 0.2$ (5 bins per decade) centered on $\log[L(\text{W Hz}^{-1})] = 19.4$ to 27.6 and calculated separate local luminosity functions of star-forming galaxies and AGNs using

$$\rho_{\text{dex}} = 5 \sum_{i=1}^N \left(\frac{1}{V_{\max}} \right)_i. \quad (26)$$

Our 1.4 GHz local luminosity functions ρ_{dex} for star-forming galaxies and AGNs are listed in Table 3 and plotted in Figure 13. The listed errors are the rms Poisson counting errors for independent galaxies

$$\sigma = 5 \left[\sum_{i=1}^N \left(\frac{1}{V_{\max}} \right)_i^2 \right]^{1/2} \quad (27)$$

quadratically summed with a 3% flux-scale uncertainty. If the number N of galaxies in a luminosity bin is small ($N < 5$), the quoted errors are the 84% confidence limits tabulated in Gehrels (1986). Clustering and cosmic variance are addressed in Section 8.

The luminosity functions of SFGs and AGNs intersect at $\log[L(1.4 \text{ GHz})] \approx 22.7$ in agreement with the earlier result of Condon et al. (2002) and close to the $\log[L(\text{W Hz}^{-1})] \approx 22.9$ found by Mauch & Sadler (2007) despite the different samples and classification methods used. This crossover marks the 1.4 GHz spectral luminosity below which star-forming galaxies outnumber AGNs within the local universe.

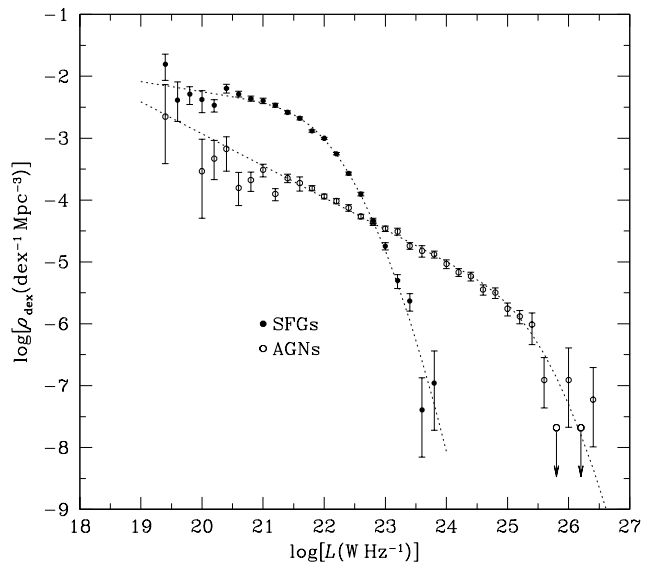


Figure 13. The 2MASX/NVSS 1.4 GHz logarithmic luminosity functions for sources whose radio emission is dominated by star formation (filled circles) and AGNs (unfilled circles). The two dotted curves represent the Saunders et al. (1990) and double power-law fits to the local luminosity functions of star-forming galaxies and AGNs, respectively.

6.4.1. Star-Forming Galaxies

The FIR/radio correlation shows that the radio and FIR luminosities of star-forming galaxies are nearly pro-

Table 3
1.4 GHz Local Luminosity Functions ($h = 0.70$)

log L (W Hz^{-1})	Star-forming Galaxies		AGNs	
	N	log ρ_{dex} ($\text{dex}^{-1} \text{Mpc}^{-3}$)	N	log ρ_{dex} ($\text{dex}^{-1} \text{Mpc}^{-3}$)
19.4	6	$-1.81^{+0.16}_{-0.26}$	1	$-2.65^{+0.52}_{-0.76}$
19.6	3	$-2.39^{+0.30}_{-0.34}$	0	...
19.8	10	$-2.29^{+0.12}_{-0.17}$	0	...
20.0	11	$-2.37^{+0.14}_{-0.21}$	1	$-3.53^{+0.52}_{-0.76}$
20.2	21	$-2.46^{+0.09}_{-0.11}$	3	$-3.33^{+0.30}_{-0.34}$
20.4	59	$-2.20^{+0.07}_{-0.08}$	5	$-3.17^{+0.20}_{-0.36}$
20.6	103	$-2.29^{+0.05}_{-0.05}$	4	$-3.80^{+0.25}_{-0.28}$
20.8	147	$-2.36^{+0.04}_{-0.04}$	9	$-3.68^{+0.13}_{-0.18}$
21.0	244	$-2.39^{+0.04}_{-0.05}$	22	$-3.51^{+0.09}_{-0.12}$
21.2	411	$-2.47^{+0.03}_{-0.03}$	22	$-3.90^{+0.09}_{-0.11}$
21.4	584	$-2.58^{+0.02}_{-0.02}$	65	$-3.65^{+0.06}_{-0.07}$
21.6	823	$-2.68^{+0.02}_{-0.02}$	85	$-3.73^{+0.10}_{-0.13}$
21.8	975	$-2.88^{+0.02}_{-0.02}$	171	$-3.81^{+0.04}_{-0.04}$
22.0	1124	$-3.00^{+0.02}_{-0.02}$	216	$-3.94^{+0.04}_{-0.04}$
22.2	893	$-3.25^{+0.02}_{-0.02}$	281	$-4.02^{+0.04}_{-0.04}$
22.4	624	$-3.57^{+0.02}_{-0.02}$	280	$-4.12^{+0.05}_{-0.06}$
22.6	368	$-3.90^{+0.03}_{-0.03}$	286	$-4.26^{+0.03}_{-0.04}$
22.8	168	$-4.34^{+0.04}_{-0.05}$	239	$-4.37^{+0.04}_{-0.05}$
23.0	87	$-4.74^{+0.05}_{-0.06}$	209	$-4.46^{+0.04}_{-0.05}$
23.2	30	$-5.30^{+0.10}_{-0.13}$	184	$-4.51^{+0.06}_{-0.06}$
23.4	13	$-5.63^{+0.12}_{-0.17}$	133	$-4.74^{+0.05}_{-0.06}$
23.6	1	$-7.39^{+0.52}_{-0.76}$	97	$-4.82^{+0.08}_{-0.10}$
23.8	1	$-6.96^{+0.52}_{-0.76}$	103	$-4.88^{+0.05}_{-0.06}$
24.0	0	...	69	$-5.03^{+0.06}_{-0.08}$
24.2	0	...	70	$-5.17^{+0.06}_{-0.07}$
24.4	0	...	59	$-5.23^{+0.06}_{-0.08}$
24.6	0	...	41	$-5.45^{+0.07}_{-0.09}$
24.8	0	...	41	$-5.50^{+0.08}_{-0.10}$
25.0	0	...	30	$-5.76^{+0.09}_{-0.12}$
25.2	0	...	24	$-5.88^{+0.10}_{-0.12}$
25.4	0	...	8	$-6.01^{+0.18}_{-0.33}$
25.6	0	...	2	$-6.91^{+0.37}_{-0.45}$
25.8	0	...	0	$\lesssim -7.68$
26.0	0	...	1	$-6.91^{+0.52}_{-0.76}$
26.2	0	...	0	$\lesssim -7.68$
26.4	0	...	1	$-7.23^{+0.52}_{-0.76}$
26.6	0	...	0	...
26.8	0	...	0	...
27.0	0	...	0	...
27.2	0	...	0	...
27.4	0	...	0	...
27.6	0	...	1	$-8.68^{+0.52}_{-0.76}$

portional, so their logarithmic radio and FIR luminosity functions should be similar in form. Saunders et al. (1990) found that the FIR ($40 \mu\text{m} < \lambda < 120 \mu\text{m}$) logarithmic luminosity function $\phi(L)$ derived from seven large samples of IRAS sources is well fit by the parametric form

$$\phi(L) = C \left(\frac{L}{L_*} \right)^{1-\alpha} \exp \left[-\frac{1}{2\sigma^2} \log^2 \left(1 + \frac{L}{L_*} \right) \right] \quad (28)$$

that approaches a power law at with slope $(1 - \alpha)$ when $L \ll L_*$ and falls like a Gaussian with $\log(L)$ when $L \gg L_*$.

Equation 28 also fits the local 1.4 GHz logarithmic luminosity function $\rho_{\text{dex}}(L)$ of star-forming galaxies very

well, in congruence with the FIR/radio correlation, and it gives a better fit than the Schechter (1976) luminosity function. The dotted curve fitting the filled points in Figure 13 has the best-fit parameters for the 2MASX/NVSS star-forming galaxies stronger than $\log[L(\text{W Hz}^{-1})] = 19.3$: $C = 3.50 \times 10^{-3} \text{dex}^{-1} \text{Mpc}^{-3}$, $L_* = 1.9 \times 10^{21} \text{W Hz}^{-1}$, $\alpha = 1.162$, and $\sigma = 0.558$. Despite the good parametric fit to the data, we have not quoted errors on these four parameters because they are so highly correlated that they “grossly overestimate the total acceptable volume of parameter space” (Saunders et al. 1990).

Mauch & Sadler (2007) used a deeper ($k_s < 12.75$) sample of 2MASX galaxies identified with NVSS sources and having 6dF spectra in a smaller area of sky ($\Omega \approx 2.16 \text{sr}$) to calculate $\rho_{\text{dex}}(L)$ in the luminosity range $19.8 \lesssim \log(L) \lesssim 23.8$ for galaxies they classified as star-forming on the basis of their optical spectra. Their fit to the Saunders et al. (1990) form in Equation 28 gave $C = 1.48 \pm 0.17 \times 10^{-3} \text{dex}^{-1} \text{Mpc}^{-3}$, $L_* = 1.5 \pm 0.5 \times 10^{21} \text{W Hz}^{-1}$, $\alpha = 1.02 \pm 0.15$, and $\sigma = 0.60 \pm 0.04$. Again, these four parameters are so highly correlated that apparently significant differences between their values and ours are not meaningful. Direct comparisons of our binned luminosity functions show that they agree within the expected errors after cosmic variance (Section 8) has been taken into account.

6.4.2. AGNs

For the high-luminosity bins in which no sources were detected, we are able to place upper limits on the space density of AGNs. Given their large radio luminosities, hypothetical sources in these empty bins would likely be volume-limited by the $k_{20\text{Fe}} = 11.75$ cutoff. The mean absolute magnitude of AGNs in our sample with $\log[L_{1.4 \text{ GHz}}(\text{W Hz}^{-1})] > 24.5$ is $\langle K_{20\text{Fe}} \rangle \approx -25.84$. We used this value to determine the maximum volume within which such a source would have $k_{20\text{Fe}} \leq 11.75$. For luminosity bins with $N = 0$, the resulting 84%-confidence = 1σ upper limit given by Poisson statistics (Gehrels 1986) is $\log[\rho_{\text{dex}}(\text{dex}^{-1} \text{Mpc}^{-3})] \lesssim -7.68$. These limits are shown by downward pointing arrows in Figure 13 and were used as additional constraints on the AGN luminosity function. Above $\log[L(\text{W Hz}^{-1})] \sim 26.4$ those limits are well above the measured data points and provide no useful constraints on the luminosity function.

A double power-law has traditionally been used to describe the local logarithmic luminosity function of AGNs:

$$\rho_{\text{dex}}(L) = \frac{C}{(L/L_*)^\alpha + (L/L_*)^\beta} \quad (29)$$

Here α is the power-law slope in the limit $L \ll L_*$ and β is the slope for $L \gg L_*$. Both C and α are well constrained by our data. However, radio-luminous AGNs are so rare in the local universe that we can only weakly constrain the local turnover luminosity L_* and high-luminosity slope β . The deeper ($k_s < 12.75$) Mauch & Sadler (2007) AGN luminosity function gives a slightly better constraint on β .

The dotted curves matching the filled and unfilled points in Figure 13 indicate the best-fitting Saunders et al. (1990) parametric luminosity functions for the

2MASX/NVSS star-forming galaxies and AGNs, respectively.

7. LOCAL 1.4 GHz SPECTRAL POWER DENSITY FUNCTIONS

The spectral power density function $u(L)$ is defined as the spectral power density generated by sources with 1.4 GHz spectral luminosities in the range L and $L + dL$:

$$u(L) \equiv L\rho(L). \quad (30)$$

The symbol u is a reminder that the dimensions of spectral power density ($\text{W Hz}^{-1} \text{Mpc}^{-3}$) are the same as those of energy density (J Mpc^{-3}). The range of spectral luminosities spanned by galaxies is so large that it is convenient to define a logarithmic spectral power density function

$$u_{\text{dex}}(L) \equiv \ln(10)Lu(L) = L\rho_{\text{dex}}(L) \quad (31)$$

equal to the spectral power density (or energy density) per decade of spectral luminosity.

To calculate $u_{\text{dex}}(L)$ we separated our galaxies into bins of logarithmic width $\Delta \log(L) = 0.2$ centered on $\log[L(\text{W Hz}^{-1})] = 19.4, 19.6, \dots, 27.6$ and counted the number N of galaxies in each bin. There are 5 bins per decade of luminosity, so each bin centered on luminosity L yields the estimate

$$u_{\text{dex}}(L) = 5 \sum_{i=1}^N \left(\frac{L}{V_{\text{max}}} \right)_i, \quad (32)$$

with rms counting uncertainty

$$\sigma = 5 \left[\sum_{i=1}^N \left(\frac{L}{V_{\text{max}}} \right)_i^2 \right]^{1/2}. \quad (33)$$

Our 1.4 GHz local power density functions for star-forming galaxies and AGNs are listed in Table 4 with rms errors equal to the quadratic sum of the rms counting uncertainty and 3%.

7.1. Star-Forming Galaxies

As expected, the local 1.4 GHz spectral power density function of star-forming galaxies is well fit by

$$u_{\text{dex}}(L) = C \left(\frac{L}{L_*} \right)^{2-\alpha} \exp \left[-\frac{1}{2\sigma^2} \log^2 \left(1 + \frac{L}{L_*} \right) \right] \quad (34)$$

with the same parameters $C = 3.50 \times 10^{-3} \text{ dex}^{-1} \text{Mpc}^{-3}$, $L_* = 1.9 \times 10^{21} \text{ W Hz}^{-1}$, $\alpha = 1.162$, and $\sigma = 0.558$ that fit the local logarithmic luminosity function. This fit is indicated by the dotted curve matching the filled circles in Figure 14.

The total 1.4 GHz spectral power produced per unit volume by star-forming galaxies U_{SF} is the integral the local power density function of star-forming galaxies over spectral luminosity:

$$U_{\text{SF}} = \int_0^\infty u_{\text{SF}}(L) dL. \quad (35)$$

U_{SF} is an extinction-free measurement proportional to the SFRD ψ_{SF} ($M_\odot \text{ yr}^{-1} \text{Mpc}^{-3}$). We calculated U_{SF}

Table 4
1.4 GHz Spectral Power Density Functions ($h = 0.70$)

$\log L$ (W Hz^{-1})	Star-forming Galaxies		AGNs	
	N	$\log u_{\text{dex}}$ ($\text{W Hz}^{-1} \text{dex}^{-1} \text{Mpc}^{-3}$)	N	$\log u_{\text{dex}}$ ($\text{W Hz}^{-1} \text{dex}^{-1} \text{Mpc}^{-3}$)
19.4	6	17.56 ^{+0.16} _{-0.25}	1	16.76 ^{+0.52} _{-0.76}
19.6	3	17.18 ^{+0.30} _{-0.34}	0	...
19.8	10	17.53 ^{+0.12} _{-0.17}	0	...
20.0	11	17.66 ^{+0.14} _{-0.22}	1	16.45 ^{+0.52} _{-0.76}
20.2	21	17.72 ^{+0.09} _{-0.11}	3	16.85 ^{+0.30} _{-0.34}
20.4	59	18.22 ^{+0.07} _{-0.08}	5	17.21 ^{+0.19} _{-0.34}
20.6	103	18.32 ^{+0.04} _{-0.05}	4	16.83 ^{+0.25} _{-0.28}
20.8	147	18.45 ^{+0.04} _{-0.04}	9	17.12 ^{+0.13} _{-0.18}
21.0	244	18.60 ^{+0.04} _{-0.04}	22	17.47 ^{+0.09} _{-0.12}
21.2	411	18.74 ^{+0.03} _{-0.03}	22	17.33 ^{+0.09} _{-0.11}
21.4	584	18.81 ^{+0.02} _{-0.02}	65	17.74 ^{+0.06} _{-0.07}
21.6	823	18.92 ^{+0.02} _{-0.02}	85	17.88 ^{+0.10} _{-0.13}
21.8	975	18.91 ^{+0.02} _{-0.02}	171	18.00 ^{+0.04} _{-0.04}
22.0	1124	19.00 ^{+0.02} _{-0.02}	216	18.06 ^{+0.04} _{-0.04}
22.2	893	18.94 ^{+0.02} _{-0.02}	281	18.19 ^{+0.04} _{-0.04}
22.4	624	18.82 ^{+0.02} _{-0.02}	280	18.29 ^{+0.05} _{-0.06}
22.6	368	18.68 ^{+0.03} _{-0.03}	286	18.33 ^{+0.03} _{-0.04}
22.8	168	18.45 ^{+0.04} _{-0.05}	239	18.43 ^{+0.04} _{-0.05}
23.0	87	18.24 ^{+0.05} _{-0.06}	209	18.54 ^{+0.04} _{-0.05}
23.2	30	17.86 ^{+0.09} _{-0.12}	184	18.69 ^{+0.05} _{-0.06}
23.4	13	17.74 ^{+0.12} _{-0.17}	133	18.65 ^{+0.06} _{-0.06}
23.6	1	16.28 ^{+0.52} _{-0.76}	97	18.80 ^{+0.09} _{-0.11}
23.8	1	16.85 ^{+0.52} _{-0.76}	103	18.92 ^{+0.05} _{-0.06}
24.0	0	...	69	18.97 ^{+0.07} _{-0.08}
24.2	0	...	70	19.03 ^{+0.06} _{-0.07}
24.4	0	...	59	19.17 ^{+0.06} _{-0.08}
24.6	0	...	41	19.15 ^{+0.07} _{-0.09}
24.8	0	...	41	19.31 ^{+0.08} _{-0.09}
25.0	0	...	30	19.25 ^{+0.10} _{-0.12}
25.2	0	...	24	19.30 ^{+0.10} _{-0.12}
25.4	0	...	8	19.36 ^{+0.12} _{-0.18}
25.6	0	...	2	18.66 ^{+0.37} _{-0.45}
25.8	0	...	0	$\lesssim 18.16$
26.0	0	...	1	19.27 ^{+0.52} _{-0.76}
26.2	0	...	0	$\lesssim 18.56$
26.4	0	...	1	19.27 ^{+0.52} _{-0.76}
26.6	0	...	0	...
26.8	0	...	0	...
27.0	0	...	0	...
27.2	0	...	0	...
27.4	0	...	0	...
27.6	0	...	1	18.88 ^{+0.52} _{-0.76}

directly by summing L/V_{max} over the unbinned sample of all star-forming galaxies in the 1.4 GHz 2MASX/NVSS spectroscopic subsample; it is

$$U_{\text{SF}} = (1.54 \pm 0.05) \times 10^{19} \text{ W Hz}^{-1} \text{Mpc}^{-3} \quad (36)$$

for $H_0 = 70 \text{ km s}^{-1} \text{Mpc}^{-1}$. The rms error in U_{SF} includes a 3% flux-density calibration uncertainty.

Let $U_{\text{SF}}(> L)$ be the cumulative spectral power density produced by star-forming galaxies with 1.4 GHz spectral luminosities $> L$, so the ratio $U_{\text{SF}}(> L)/U_{\text{SF}}$ is the fraction of U_{SF} produced by galaxies more luminous than L . The curve in Figure 15 shows that ratio calculated from our fit to Equation 34. It is 0.99 for $\log[L(\text{W Hz}^{-1})] = 19.3$, the lowest luminosity in the

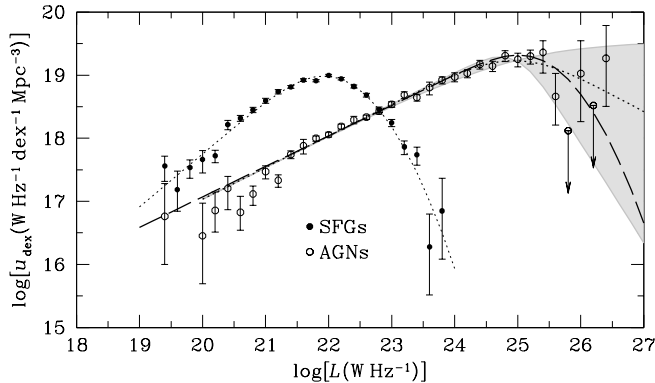


Figure 14. Local spectral power density functions for radio sources powered primarily by star formation (filled circles) and AGNs (open circles) derived from the 2MASX/NVSS spectroscopic sample shown as functions of radio luminosity $L_{1.4\text{ GHz}}$. The SFGs were fitted by the Saunders et al. (1990) parametric form (Equation 28) multiplied by $L_{1.4\text{ GHz}}$. The AGNs were fitted by both the Saunders et al. (1990) form (dashed curve) and by the Equation 29 double power law (dotted curve). The shaded region shows the wide range of possible slopes β in Equation 29 such that $\chi^2 < 2$.

2MASX/NVSS spectroscopic subsample, suggesting that sources fainter than our sample limit account for $< 1\%$ of all nearby star formation.

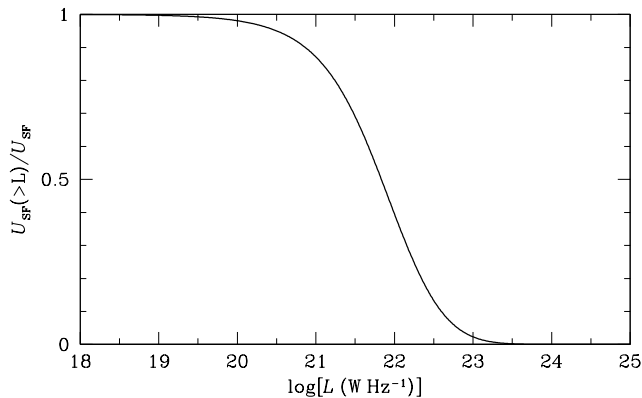


Figure 15. This curve shows the fraction $U_{\text{SF}}(>L)/U_{\text{SF}}$ of the 1.4 GHz spectral power density generated by star-forming galaxies with luminosities $> L$ predicted by extrapolating the fitting function in Equation 34.

7.2. AGNs

Excluding the anomalous quasar 3C 273 at $\log[L(\text{W Hz}^{-1})] \sim 27.4$, the parameters of the double power-law fit were determined by minimizing the reduced χ^2 statistic of the fit to the measurements weighted by their uncertainties. The dashed line in Figure 14 represents this best fit to Equation 29 with parameters $C = 3.58 \times 10^{-6}$, $L_* = 9.55 \times 10^{24} \text{ W Hz}^{-1}$, $\alpha = 0.498$, and $\beta = 1.55$. Because luminous AGNs are so rare, the value for β can range from 1 to 2.58 for $\chi^2 < 2$ (shaded region in Figure 14).

Lacking the data needed to constrain the high-luminosity power-law slope β for the AGN luminosity function, we considered an alternative approach. There is strong evidence supporting the notion of co-evolution

of star-forming host galaxies and AGNs (e.g. Gebhardt et al. 2000). This co-evolution indicates that the luminosity functions of these populations might be represented by the same functional form, so we applied the Saunders et al. (1990) form (Equation 28) used for the SFGs to the AGNs. There remains the issue of the poorly sampled high- L end of the AGN luminosity function, so we held our SFG value $\sigma = 0.558$ fixed while fitting the AGN luminosity function. The dotted curve following the unfilled points in Figure 13 represents the best-fitting Equation 28 parameters for the 2MASX/NVSS AGNs: $C = 4.59 \times 10^{-6} \text{ dex}^{-1} \text{ Mpc}^{-3}$, $L_* = 4.65 \times 10^{24} \text{ W Hz}^{-1}$, $\alpha = 1.516$, and $\sigma = 0.558$.

We calculated the total 1.4 GHz spectral power density produced by AGNs U_{AGN} directly by summing L/V_{max} over the unbinned sample of all AGNs in 1.4 GHz 2MASX/NVSS spectroscopic subsample; it is

$$U_{\text{AGN}} = (4.23 \pm 0.55) \text{ W Hz}^{-1} \text{ Mpc}^{-3} \quad (37)$$

for $H_0 = 70 \text{ km s}^{-1} \text{ Mpc}^{-1}$. The rms error in U_{AGN} includes a 3% flux-density calibration uncertainty.

8. COSMIC VARIANCE

The small statistical errors quoted in Tables 3 and 4 and in Equations 36 and 37 include only the Poisson counting errors for unclustered galaxies added in quadrature with the 3% absolute flux-density calibration uncertainty of the NVSS (Condon et al. 1998). The mean accessible redshifts of galaxies used to estimate the local spectral luminosity and power density functions, weighted by each source’s contribution to the total star formation density, are $\langle z \rangle = 0.026$ and $\langle z \rangle = 0.070$ for the 2MASX/NVSS star-forming galaxies and AGNs, respectively. The corresponding distances $D \sim 100 - 300 \text{ Mpc}$ are comparable with the size $D \sim 150 \text{ Mpc}$ of baryon acoustic oscillations, so significant cosmic variance from large-scale clustering is expected. To extend our local results (e.g., the local U_{SF}) derived from observations made from only one point in the universe to the whole universe (e.g, the recent U_{SF} averaged over all space), it is necessary to add this cosmic variance to the Poisson and calibration variances.

To estimate the amplitude of the cosmic variance, we divided our sample covering 7.016 sr of the sky into two equal-area hemispheres split by the vertical plane passing through J2000 $\alpha = 12^{\text{h}}51^{\text{m}}26^{\text{s}}$, the right ascension of the north galactic pole (Figure 16). We call the hemisphere covering J2000 $\alpha = 00^{\text{h}}51^{\text{m}}26^{\text{s}}$ through $\alpha = 12^{\text{h}}51^{\text{m}}26^{\text{s}}$ “RA1” and the other hemisphere “RA2.”

The 3603 star-forming galaxies in RA1 produce $U_{\text{SF},1} = (1.75 \pm 0.06) \times 10^{19} \text{ W Hz}^{-1} \text{ Mpc}^{-3}$ and the 3103 star-forming sources in RA2 produce $U_{\text{SF},2} = (1.35 \pm 0.04) \times 10^{19} \text{ W Hz}^{-1} \text{ Mpc}^{-3}$, where these errors do not include cosmic variance. The fractional difference in U_{SF} between the two hemispheres is actually ~ 0.26 , so if the two halves of the sky are nearly independent, the rms fractional uncertainty in their mean is ~ 0.13 . Thus our spectroscopic subsample is large enough that cosmic variance exceeds its Poisson and calibration variances. Our estimate of the recent “universal” U_{SF} based on local measurements must include the cosmic variance; it

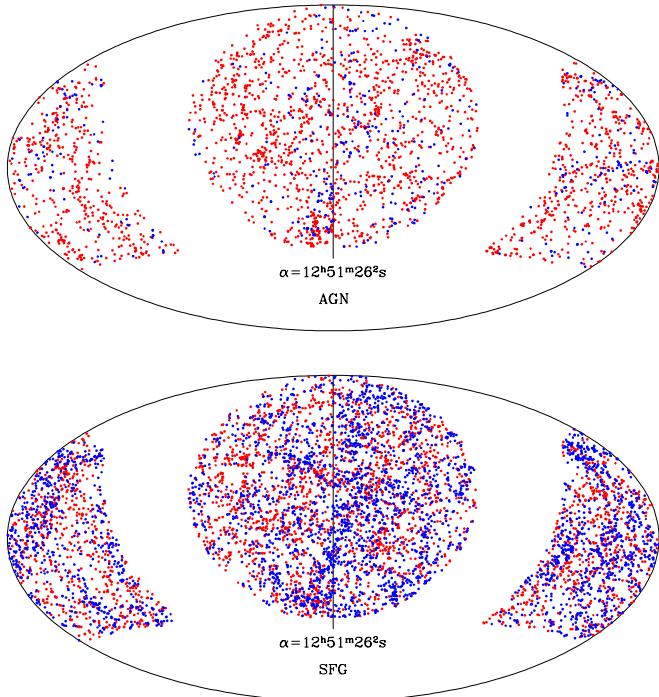


Figure 16. AGNs (upper panel) and SFGs (lower panel) in our sample are shown on Hammer equal-area projections of the sky centered on J2000 $\alpha = 12^{\text{h}}51^{\text{m}}26^{\text{s}}$ and $\delta = 0$. Right ascension increases to the left, so the RA1 hemisphere is to the right of the vertical dividing line and the RA2 hemisphere is to the left. Blue indicates galaxies with $cz < 7000 \text{ km s}^{-1}$, and $cz > 7000 \text{ km s}^{-1}$ galaxies are red. The color boundary at $cz = 7000 \text{ km s}^{-1}$ corresponds to a distance $D \sim 100 \text{ Mpc}$.

is

$$U_{\text{SF}} = (1.54 \pm 0.20) \times 10^{19} \text{ W Hz}^{-1} \text{ Mpc}^{-3}. \quad (38)$$

The corresponding numbers for radio sources primarily powered by AGNs are $U_{\text{AGN},1} = (4.72 \pm 0.55) \times 10^{19} \text{ W Hz}^{-1} \text{ Mpc}^{-3}$ and $U_{\text{AGN},2} = (3.74 \pm 0.53) \times 10^{19} \text{ W Hz}^{-1} \text{ Mpc}^{-3}$, so adding the cosmic variance implies the recent universal AGN spectral energy density is

$$U_{\text{AGN}} = (4.23 \pm 0.78) \times 10^{19} \text{ W Hz}^{-1} \text{ Mpc}^{-3}. \quad (39)$$

Figure 16 suggests that bisecting the sky at the chosen meridian gives a larger difference than most other choices would have, so we believe the overall error estimates in Equations 38 and 39 are conservative.

Figures 13 and 14 show our luminosity and power-density function data points with error bars that do not include cosmic variance. We note that the data still match, within those small error bars, the smooth parametric fits shown as dotted curves. We conclude that cosmic variance affects the overall space density of galaxies but not their detailed luminosity distributions.

We can also use our local sample to estimate how the expansion dynamics of a Λ CDM universe might be affected by density fluctuations on small scales. The $\lambda = 2.16 \mu\text{m}$ spectral luminosity densities of our sample galaxies in RA1 and RA2 are $1.734 \times 10^{20} \text{ W Hz}^{-1} \text{ Mpc}^{-3}$ and $1.065 \times 10^{20} \text{ W Hz}^{-1} \text{ Mpc}^{-3}$, respectively. Using the $\lambda = 2.16 \mu\text{m}$ luminosity as a proxy for baryonic mass and

assuming dark matter has a similar large-scale distribution, relative to the mean matter density, RA1 and RA2 have densities 1.239 and 0.761. For the global cosmological parameters $\Omega_m = 0.3$, $\Omega_\Lambda = 0.7$, and $\Omega_r = 8.5 \times 10^{-5}$,

$$\Omega_{\text{RA1}} = (0.3 \times 1.239 + 0.7 + 8.6 \times 10^{-5}) = 1.0718$$

$$\Omega_{\text{RA2}} = (0.3 \times 0.761 + 0.7 + 8.6 \times 10^{-5}) = 0.9284.$$

The “local” Hubble constant is proportional to $\Omega^{1/2}$, so in regions RA1 and RA2 the local Hubble constant could be $H_{0,1} \approx 72.5 \text{ km s}^{-1} \text{ Mpc}^{-1}$ and $H_{0,2} = 67.5 \text{ km s}^{-1} \text{ Mpc}^{-1}$. This scatter is comparable to that of published values of H_0 , with the difference being that the lower published value is a global measurement rather than a small-scale measurement such as this. Regardless, differing densities on $\sim 100 \text{ Mpc}$ scales may prevent local measurements of the global H_0 to better than $\sim \pm 2.5 \text{ km s}^{-1}$.

9. RECENT STAR FORMATION RATE DENSITY

Radio continuum emission is a tight, nearly linear, and dust-unbiased independent tracer of the SFRD ψ . Steep-spectrum ($\langle \alpha \rangle \approx -0.8$) synchrotron radiation from relativistic electrons accelerated in the core-collapse SNRs of short-lived massive ($M > 8 M_\odot$) stars dominates the radio emission of SFGs at all frequencies below $\nu \sim 30 \text{ GHz}$, and flat-spectrum ($\alpha \approx -0.1$) free-free radiation from thermal electrons in H II regions ionized by even more massive short-lived stars emerges above 30 GHz (Condon 1992). At $\nu \sim 1 \text{ GHz}$, $\sim 90\%$ of the radio emission from SFGs can be attributed to synchrotron radiation and the remaining $\sim 10\%$ to free-free emission. The FIR/radio correlation shows that SFR is proportional to radio luminosity in all but the least-luminous SFGs (Condon et al. 1991), indicating that the constant of proportionality between radio luminosity and SFR is remarkably insensitive to potentially confounding variables such as interstellar magnetic field strength.

Thus SFR can be related to 1.4 GHz luminosity by an equation of the form

$$\frac{\text{SFR}(M > 5 M_\odot)}{M_\odot \text{ yr}^{-1}} = \frac{1}{x} \left(\frac{L_{1.4 \text{ GHz}}}{\text{W Hz}^{-1}} \right), \quad (40)$$

where x is a dimensionless constant whose value has been found to range from $\sim 1.8 \times 10^{21}$ to $\sim 8.9 \times 10^{21}$. For example, (Condon et al. 2002) reported

$$\frac{\text{SFR}(M > 5 M_\odot)}{M_\odot \text{ yr}^{-1}} = \frac{1}{4.6 \times 10^{21}} \left(\frac{L_{1.4 \text{ GHz}}}{\text{W Hz}^{-1}} \right). \quad (41)$$

Radio emission is insensitive to lower-mass stars. To account for their contribution to the total star-formation rate, we followed Madau & Dickinson (2014) and assumed a Salpeter initial mass function $\Psi(M) \propto M^{-2.35}$ over the mass range $0.1 M_\odot < M < 100 M_\odot$. Then the total star-formation rate is

$$\text{SFR}(M > 0.1 M_\odot) \approx 5.5 \text{ SFR}(M > 5 M_\odot). \quad (42)$$

Because the conversion factor between 1.4 GHz luminosity and total SFR is still uncertain, with values ranging from $5.5x \sim 0.8 \times 10^{21}$ to 1.7×10^{21} , we adopted the easily rescalable midrange number 1.0×10^{-21} . Dividing

SFR and 1.4 GHz luminosity by volume gives the SFRD ψ in terms of U_{SF} :

$$\frac{\psi(M > 0.1 M_{\odot})}{M_{\odot} \text{ yr}^{-1} \text{ Mpc}^{-3}} \approx 1.0 \times 10^{-21} \left(\frac{U_{\text{SF}}}{\text{W Hz}^{-1} \text{ Mpc}^{-3}} \right). \quad (43)$$

Then our measured $U_{\text{SF}} = (1.54 \pm 0.20) \times 10^{19} \text{ W Hz}^{-1}$ with the quoted error including cosmic variance implies that the “universal” recent SFRD is

$$\psi = (0.0154 \pm 0.0020) M_{\odot} \text{ yr}^{-1} \text{ Mpc}^{-3}. \quad (44)$$

This value of ψ is lower than the $\psi = (0.022 \pm 0.001) M_{\odot} \text{ yr}^{-1} \text{ Mpc}^{-3}$ (Poisson errors only) Mauch & Sadler (2007) calculated using the higher conversion factor $\psi = 1.13 \times 10^{-21} U_{\text{SF}}$. However, rescaling their conversion factor to $\psi = 1.0 \times 10^{-21} U_{\text{SF}}$ and adding cosmic variance to their rms uncertainty yields $\psi = 0.0195 \pm 0.0036 M_{\odot} \text{ yr}^{-1} \text{ Mpc}^{-3}$. Thus these two measurements of ψ agree within their uncertainties.

Multiwavelength compilations of SFRD estimates can be found in Hopkins & Beacom (2006) and Madau & Dickinson (2014). After scaling to the Salpeter IMF, Hopkins & Beacom (2006) adopted the Cole et al. (2001) parametric fit to describe the evolution of the SFRD over the redshift range $0 < z < 7$:

$$\psi(z) = \frac{(a + bz)h}{1 + (z/c)^d} M_{\odot} \text{ yr}^{-1} \text{ Mpc}^{-3}. \quad (45)$$

For $h = 0.7$ they found $a = 0.0170$, $b = 0.13$, $c = 3.3$, and $d = 5.3$. At the weighted average redshift $\langle z \rangle \sim 0.026$ of our SFG sample, Equation 45 yields $\psi = 0.015 M_{\odot} \text{ yr}^{-1} \text{ Mpc}^{-3}$. From a compilation of FUV and IR rest-frame measurements of ψ spanning $0 < z < 8$, Madau & Dickinson (2014) found the best-fit function

$$\psi(z) = 0.015 \frac{(1+z)^{2.7}}{1 + [(1+z)/2.9]^{5.6}} M_{\odot} \text{ yr}^{-1} \text{ Mpc}^{-3}. \quad (46)$$

Equation 46 gives $\psi(0.026) = 0.016 M_{\odot} \text{ yr}^{-1} \text{ Mpc}^{-3}$. Our $\psi = 0.0154 \pm 0.020 M_{\odot} \text{ yr}^{-1} \text{ Mpc}^{-3}$ centered on $\langle z \rangle \approx 0.026$ agrees with both of these independent SFRD evolutionary models. The blue point in Figure 17 compares our measurement with the FIR and UV data points and the dashed curve showing the Madau & Dickinson (2014) model.

This publication made use of data products from the

Two Micron All Sky Survey, which is a joint project of the University of Massachusetts and the Infrared Processing and Analysis Center/California Institute of Technology, funded by the National Aeronautics and Space Administration and the National Science Foundation. This research made use of the NASA/IPAC Extragalactic Database (NED), which is operated by the Jet Propulsion Laboratory, California Institute of Technology, under contract with the National Aeronautics and Space Administration. This publication made use of data products from the Wide-field Infrared Survey Explorer, which is a joint project of the University of California, Los Angeles, and the Jet Propulsion Laboratory/California Institute of Technology, funded by the National Aeronautics and Space Administration. This material is based

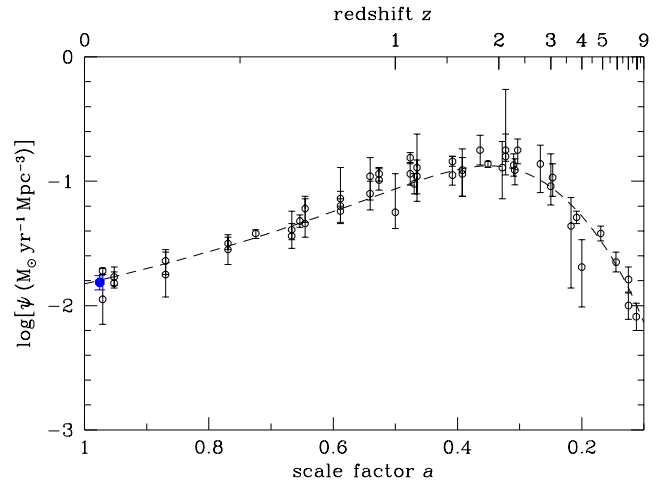


Figure 17. The Madau & Dickinson (2014) SFRD model (Equation 46) is indicated by the dashed curve fitted to their black FIR and UV data points. The blue data point at expansion scale factor $a = (1+z)^{-1} \sim 0.98$ ($z = 0.026$) represents our estimate of the recent SFRD from based on U_{SF} measured at 1.4 GHz. Lower abscissa: expansion scale factor $a = (1+z)^{-1}$. Upper abscissa: redshift z . Ordinate: star formation rate density ($M_{\odot} \text{ yr}^{-1} \text{ Mpc}^{-3}$).

upon work supported by the National Science Foundation Graduate Research Fellowship under Grant No. DDGE-1315231.

We thank our anonymous referee for a careful reading and exceptionally valuable suggestions for improving this paper.

APPENDIX

A. 2MASX/NVSS SKY COVERAGE

The 2MASX/NVSS sample covers the sky with J2000 $\delta > \delta_0 = -40^\circ$ except for absolute galactic latitudes $|b| < b_0 = 20^\circ$. The sample solid angle is the solid angle with $\delta > \delta_0$ minus the solid angle with $|b| < b_0$, except for (therefore plus) the solid angle with $|b| < b_0$ and δ_0 :

$$\Omega = \Omega(\delta > \delta_0) - \Omega(|b| < b_0) + \Omega(|b| < b_0, \delta < \delta_0). \quad (A1)$$

On a unit sphere the Cartesian coordinates corresponding to the J2000 equatorial coordinates α, δ are

$$\begin{aligned} x &= \sin \alpha \cos \delta \\ y &= \cos \alpha \cos \delta \\ z &= \sin \delta \end{aligned} \quad (A2)$$

The circle of constant declination δ has radius $r = (x^2 + y^2)^{1/2} = \cos \delta$, so the solid angle covering all right ascensions α and declinations north of $\delta_0 = -40^\circ$ is

$$\Omega(\delta > \delta_0) = 2\pi \int_{\delta_0}^{\pi/2} \cos \delta \, d\delta = 2\pi(1 - \sin \delta_0) \approx 10.3219 \text{ sr} \quad (\text{A3})$$

Likewise, the band covering all galactic longitudes l and absolute galactic latitudes $|b| < b_0 = 20^\circ$ covers solid angle

$$\Omega(|b| < b_0) = 2\pi \int_{-b_0}^{b_0} \cos b \, db = 4\pi \sin b_0 \approx 4.2980 \text{ sr} \quad (\text{A4})$$

The third term of Equation A1 is the solid angle with $|b| < b_0$ and $\delta < \delta_0$. It can be written in the form

$$\Omega(\delta < \delta_0, |b| < b_0) = \int_{-b_0}^{b_0} \cos b \int_{l_{\min}(b)}^{l_{\max}(b)} dl \, db \quad (\text{A5})$$

where $l_{\max}(b) - l_{\min}(b)$ is the range of galactic longitudes at galactic latitude b and declination δ . Calculating that range requires converting between equatorial and galactic coordinates.

The J2000 equatorial coordinates of the North Galactic Pole (NGP) are $\alpha_p = 12^{\text{h}}51^{\text{m}}26^{\text{s}}$ and $\delta_p = +27^\circ 7' 42'' \approx 27.1283 \text{ deg.}^2$ The 2MASX/NVSS region spans all α , so only δ_p matters. We can define “shifted” galactic coordinates (λ, b) with $\alpha_p = 0$ so converting from (α, δ) to (λ, b) needs only a single rotation about the x axis and

$$\begin{aligned} x &= \sin \lambda \cos b \\ y &= \cos \lambda \cos b \\ z &= \sin b \end{aligned} \quad (\text{A6})$$

Counterclockwise rotation through any angle ψ about the x axis yields new coordinates

$$\begin{aligned} x' &= x \\ y' &= y \cos \psi + z \sin \psi \\ z' &= z \cos \psi - y \sin \psi \end{aligned} \quad (\text{A7})$$

Rotating these coordinates *clockwise* by the codeclination of the galactic pole $(\pi/2 - \delta_p)$ corresponds to $\psi = (\delta_p - \pi/2)$. Thus the three equations for λ, b as functions of α, δ , and ψ are:

$$\begin{aligned} x' &= \sin \lambda \cos b = \sin \alpha \cos \delta \\ y' &= \cos \lambda \cos b = (\cos \alpha \cos \delta) \cos \psi + \sin \delta \sin \psi \\ z' &= \sin b = \sin \delta \cos \psi - (\cos \alpha \cos \delta) \sin \psi \end{aligned} \quad (\text{A8})$$

Solving the z' equation for

$$(\cos \alpha \cos \delta) = \frac{\sin \delta \cos \psi - \sin b}{\sin \psi} \quad (\text{A9})$$

and substituting this into the y' equation gives

$$\cos \lambda \cos b = \left(\frac{\sin \delta \cos \psi - \sin b}{\sin \psi} \right) \cos \psi + \sin \delta \sin \psi \quad (\text{A10})$$

The longitude $\lambda(b, \delta_0)$ at which galactic latitude b crosses J2000 declination δ_0 is

$$\lambda(b, \delta_0) = \arccos \left[\left(\frac{\sin \delta_0 \cos \psi - \sin b}{\sin \psi \cos b} \right) \cos \psi + \frac{\sin \delta_0 \sin \psi}{\cos b} \right] \quad (\text{A11})$$

Thus Equation A5 becomes

$$\Omega(\delta < \delta_0, |b| < b_0) = \int_{-b_0}^{b_0} 2\lambda(b, \delta_0) \cos b \, db \quad (\text{A12})$$

in (λ, b) coordinates. Integrating Equation A12 numerically for $\delta_0 = -40^\circ$ and $b_0 = 20^\circ$ gives $\Omega(\delta < \delta_0, |b| < b_0) \approx 0.9920 \text{ sr}$. Inserting Equations A3, A4, and this result into Equation A1 gives the total 2MASX/NVSS solid angle $\Omega \approx 7.0160 \text{ sr}$.

² <http://astronomy.swin.edu.au/cosmos/N/North+Galactic+Pole>

B. NEW SPECTROSCOPIC REDSHIFTS

We obtained spectra for 12 of the 19 galaxies lacking published spectroscopic redshifts with the Dual Imaging Spectrograph (DIS) on the Apache Point Observatory (APO) 3.5 m telescope. Observations were carried out over three half-nights occurring in October through December of 2017. DIS is a medium dispersion double spectrograph that has separated red and blue channels. The standard “high” resolution DIS III grating setup B1200/R1200 was used. The wavelength ranges were centered on the $H\beta$ and $H\alpha$ lines at the median redshift of the 2MASX/NVSS sample, 5021 Å and 6780 Å for the blue and red cameras, respectively. This resulted in a wavelength coverage of 4401 – 5641 Å and 6200 – 7360 Å for the blue and red channels, respectively.

Total exposure times ranged from 1620 s to 3360 s, taken in intervals of 120 s to 420 s so as to mitigate cosmic-ray contamination. The two galaxies with the weakest spectral lines were observed on multiple nights to increase exposure time and improve the quality of the redshift measurement. Bias and flat frames were obtained before each observing run. Comparison spectra were obtained before and after each observation run using a He, Ne, and Ar lamp.

The spectra were reduced and analyzed in a uniform manner with IRAF. Initial 2D frames were bias-subtracted and flat-fielded using subroutines in the CCDRED package. Apertures were extracted with the APEXTRACT package. Dispersion functions were derived from the HeNeAr lamp spectra and fit to the object frames using routines in the ONEDSPEC package. Multiple sub-exposures of each target were combined for the blue and red spectra.

The blue and red portions of the spectrum were combined and processed using the XCSAO procedure in the RVSAO package to determine barycentric radial velocities. Sample spectra are shown in the top portion of Figure 18. The XCSAO routine follows the cross-correlation technique developed by Tonry & Davis (1979). We used the SDSS galaxy templates³, specifically 23–28, in the cross-correlation. Hot pixels and the unobserved wavelength range between the blue and red cameras were ignored by the cross-correlation routine. Typical results from the cross-correlation technique are shown in the bottom panel of Figure 18 for the two galaxies shown in the top panel. The resulting barycentric radial velocities are given in Table 5.

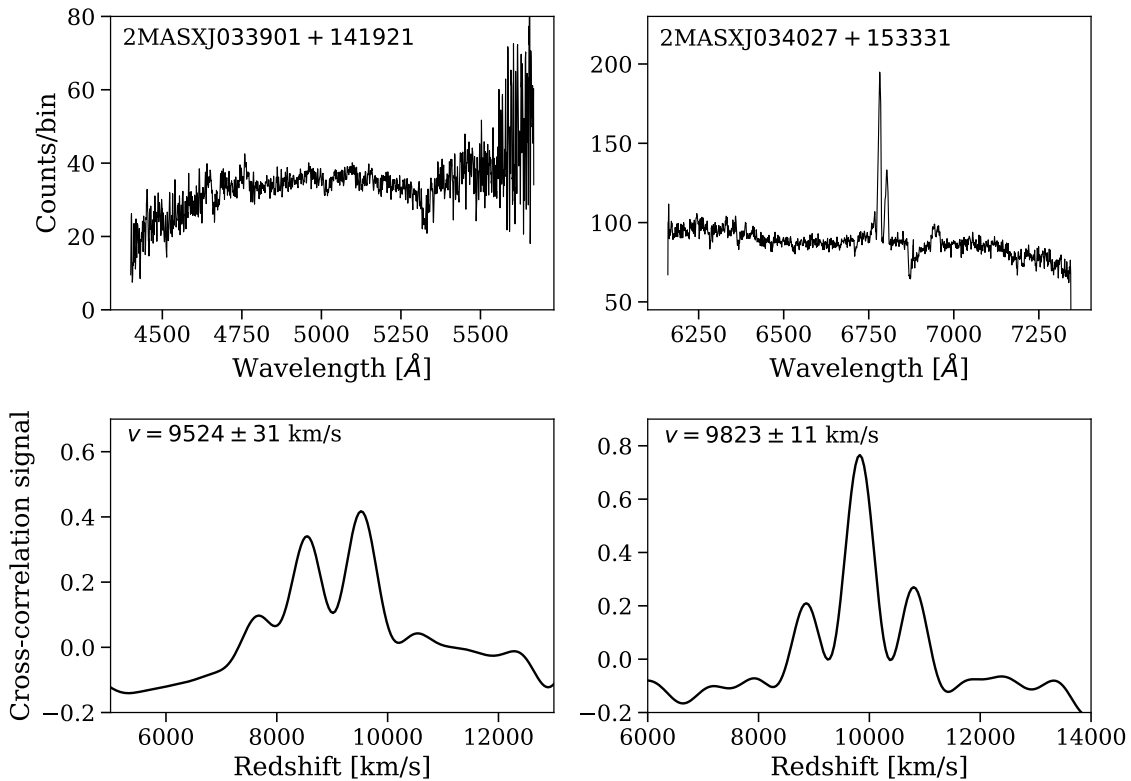


Figure 18. Top panels: Examples of typical spectra obtained for the 12 galaxies with the APO 3.5 m telescope. Left: Absorption line spectrum with the DIS blue camera. Right: Emission line spectrum with the DIS red camera. Bottom panels: Results of the cross-correlation technique used to measure the redshifts for the corresponding top panel galaxies.

The reliability of the velocities can be estimated by the r statistic, a confidence measure. Calibration done in the development of the XCSAO cross-correlation routine (Kurtz & Mink 1998) suggests that cross-correlations with $r > 3$ can be deemed reliable, but note that many of the spectra in their test study with $2 < r < 3$ also yield correct velocities. Of the twelve galaxies observed, all but one of the spectra has $r > 3$. The exception, 2MASX J21352090+8906537, has $r = 2.55$ for the template with the highest cross-correlation signal.

³ <http://classic.sdss.org/dr7/algorithms/spectemplates/>

Table 5
2MASS Supplemental Velocities

2MASX J2000 name	R.A. hh:mm:ss.ss	Dec. dd:mm:ss.s	l (deg)	b (deg)	$v = cz$ (km s ⁻¹)	σ_v (km s ⁻¹)
02570403+2000446	02:57:04.03	+20:00:44.6	159.08	-33.90	9500.6	14.4
03215557+2149375	03:21:55.57	+21:49:37.5	163.32	-29.00	14302.0	12.2
03390103+1419217	03:39:01.03	+14:19:21.7	172.61	-31.94	9523.9	31.0
03402770+1533113	03:40:27.70	+15:33:11.3	171.90	-30.82	9823.3	11.1
04141963+2025240	04:14:19.63	+20:25:24.0	174.24	-21.65	6316.2	59.9
07134975+8729044	07:13:49.75	+87:29:04.4	125.75	+27.35	15157.5	59.9
17272375+1521110	17:27:23.75	+15:21:11.0	37.88	+25.37	9045.2	37.3
17494097+5333541	17:49:40.97	+53:33:54.1	81.29	+30.50	28187.3	161.8
17543888+6803287	17:54:38.88	+68:03:28.7	98.12	+30.30	23869.6	83.9
20510128-1710242	20:51:01.28	-17:10:24.2	29.78	-33.95	19387.9	82.2
21352090+8906537	21:35:20.90	+89:06:53.7	122.18	+26.55	21094.2 ^a	125.0
23074944-1236479	23:07:49.44	-12:36:47.9	58.71	-61.74	20378.2	37.0

Note. — All velocities in reference to the Solar System barycenter.

^a Cross-correlation with the SDSS templates resulted in a R value less than 3 ($R = 2.55$).

REFERENCES

- Baldwin, J. A., Phillips, M. M., & Terlevich, R. 1981, *PASP*, 93, 5
- Best, P. N., Kauffmann, G., Heckman, T. M., Brinchmann, J., Charlot, S., Ivezić, Ž., & White, S. D. M. 2005, *MNRAS*, 362, 25
- Bell, E. F., McIntosh, D. H., Katz, N., & Weinberg, M. D. 2003, *ApJS*, 149, 289
- Best, P. N., & Heckman, T. M. 2012, *MNRAS*, 421, 1569
- Carrick, J., Turnbull, S. J., Lavaux, G., & Hudson, M. J. 2015, *MNRAS*, 450, 317
- Cole, S., Norberg, P., Baugh, C. M., et al. 2001, *MNRAS*, 326, 255
- Condon, J. J. 1984, *ApJ*, 287, 461
- Condon, J. J. 1987, *ApJS*, 65, 485
- Condon, J. J. 1992, *ARA&A*, 30, 575
- Condon, J. J., Anderson, M. L., & Helou, G. 1991, *ApJ*, 376, 95
- Condon, J. J., Balonek, T. J., & Jauncey, D. L. 1975, *AJ*, 80, 885
- Condon, J. J., Cotton, W. D., & Broderick, J. J. 2002, *AJ*, 124, 675
- Condon, J. J., Cotton, W. D., Greisen, E. W., et al. 1998, *AJ*, 115, 1693 (NVSS)
- Condon, J. J., & Matthews, A. M. 2018, *PASP*, 130, 073001
- de Grijp, M. H. K., Miley, G. K., Lub, J., & de Jong, T. 1985, *Nature*, 314, 240
- Fisher, K. B., Davis, M., Strauss, M. A., Yahil, A., & Huchra, J. 1994, *MNRAS*, 266, 50
- Fixsen, D. J., Cheng, E. S., Gales, J. M., et al. 1996, *ApJ*, 473, 576
- Gebhardt, K., Bender, R., Bower, G., et al. 2000, *ApJ*, 539, L13
- Gehrels, N. 1986, *ApJ*, 303, 336
- Geréb, K., Morganti, R., Oosterloo, T. A., Hoppmann, L., & Staveley-Smith, L. 2015, *A&A*, 580, A43
- Helou, G., Khan, I. R., Malek, L., & Boehmer, L. 1988, *ApJS*, 68, 151
- Hopkins, A. M., & Beacom, J. F. 2006, *ApJ*, 651, 142
- Huchra, J. P., Macri, L. M., Masters, K. L., et al. 2012, *ApJS*, 199:26
- Hummel, E. 1981, *A&A*, 93, 93
- Jarrett, T. 2004, *PASA*, 21, 396
- Jarrett, T. H., Chester, T., Cutri, R., et al. 2000, *AJ*, 119, 2498
- Jarrett, T. H., Cohen, M., Masci, F., et al. 2011, *ApJ*, 735:112
- Kochanek, C. S., Pahre, M. A., Falco, E. E., et al. 2001, *ApJ*, 560, 566
- Kurtz, M. J., & Mink, D. J. 1998, *PASP*, 110, 934
- Madau, P., & Dickinson, M. 2014, *ARA&A*, 52, 415
- Mauch, T., & Sadler, E. M. 2007, *MNRAS*, 375, 931
- Moshir, M., Kopman, G., & Conrow, T. A. O. 1992. Explanatory Supplement to the IRAS Faint Source Survey, Version 2 (JPL D-10015; Pasadena: Jet Propulsion Laboratory) (FSC)
- Murphy, E. J., Helou, G., Kenney, J. D. P., Armus, L., & Braun, R. 2008, *ApJ*, 678, 828
- Norris, R. P., Hopkins, A. M., Afonso, J. et al. 2011, *PASA*, 28, 215
- Owen, F. N., & Ledlow, M. J. 1997, *ApJS*, 108, 41
- Owen, F. N., White, R. A., & Ge. J. 1993, *ApJS*, 87, 135
- Parma, P., Ekers, R. D., & Fanti, R. 1985, *A&AS*, 59, 511
- Sadler, E. M., Jackson, C. A., Cannon, R. D., et al. 2002, *MNRAS*, 329, 227
- Saunders, W., Rowan-Robinson, M., Lawrence, A., et al. 1990, *MNRAS*, 242, 318
- Schechter, P. 1976, *ApJ*, 203, 297
- Skrutskie, M. F., Cutri, R. M., Stiening, R., et al. 2006, *ApJ*, 131, 1163
- Tonry, J., & Davis, M. 1979, *AJ*, 84, 1511
- van der Kruit, P. C., Oort, J. H., & Mathewson, D. S. 1972, *A&A*, 21, 169
- Wright, E. L., Eisenhardt, P. R. M., Mainzer, A. K., et al. 2010, *AJ*, 140, 1868
- Yun, M. S., Reddy, N. A., & Condon, J. J. 2001, *ApJ*, 554, 803